Journal of Materials Chemistry A

Solution-processed metal-oxide thin films for electronic and energy applications: unique chemistries of metal-nitrate precursors

Journal:	*Journal of Materials Chemistry A*
Manuscript ID	TA-REV-07-2019-007727.R1
Article Type:	Review Article
Date Submitted by the Author:	14-Sep-2019
Complete List of Authors:	Cochran, Elizabeth; University of Oregon, Department of Chemistry and Biochemistry; University of Oregon Woods, Keenan; University of Oregon, Chemistry and Biochemistry Johnson, Darren; University of Oregon, Department of Chemistry and Biochemistry Page, Catherine; University of Oregon, Chemistry and Biochemistry Boettcher, Shannon; University of Oregon,

Unique chemistries of metal-nitrate precursors to form metal-oxide thin films from solution: materials for electronic and energy applications

Elizabeth A. Cochran, Keenan N. Woods, Darren W. Johnson,*
Catherine J. Page,* Shannon W. Boettcher*

Department of Chemistry and Biochemistry, the Materials Science Institute, and the Center for Sustainable Materials Chemistry, University of Oregon, Eugene, Oregon 97403-1253, United States

Abstract

Metal-oxide thin films are used extensively in electronic and energy applications. Solution processing offers a potentially scalable and inexpensive deposition method to expand the applications of metal-oxide films and to complement vacuum-deposition techniques. Among precursors for solution deposition, metal nitrates stand out for their ability to form high-quality metal-oxide thin films. This review focuses on unique aspects of metal-nitrate chemistry that have been exploited to advance the development of solution-processed thin films. We discuss the solid-state bulk, solution, and thin-film chemical reactions involving metal nitrates and illustrate how the resulting metal-oxide thin-film properties depend on the entire reaction pathway. To conclude, we offer perspective as to how understanding the chemistry of film formation from metal-nitrate precursors is useful for addressing the primary drivers for industrial manufacturing of solution-processed metal-oxide thin films.

1. Introduction

The versatility of metal-oxide thin films make them useful for applications in electronic and energy technologies. Metal oxides are utilized as dielectric,[1,2] semiconductor,[1,3] or metal components (i.e. transparent conducting oxides)[4,5] of thin-film transistors (TFTs) and photovoltaic cells.[6,7] In photovoltaics, metal oxides can also serve as carrier-selective contacts to improve solar-cell efficiencies (silicon, perovskite, organic, etc.), examples of which include TiO_2[8–10] and ZnO[10–12] for electron-selective contacts and MoO_x[13,14] and NiO[15,16] for hole-selective contacts. Additional applications include smart windows,[17,18] solid-oxide fuel cells,[19–21] protective layers,[22] and catalysis, as both active[23,24] and support[25,26] materials for renewable fuel production.

Conventional vapor-phase deposition methods produce high-quality metal-oxide thin films for many of the above-mentioned applications, but face inherent challenges in large-area deposition critical for "macroelectronics," which require the use of substrates much larger than semiconductor fabrication facilities currently accommodate.[27] For this reason, solution processing offers opportunity for growth in macroelectronic technology sectors (e.g. photovoltaics, displays, and "smart" window coatings). The benefits of solution processing relative to vapor-phase deposition include potentially lower cost, processing under ambient conditions, simple composition tuning, and the use of environmentally benign solvents/precursors.[27]

Solution-processed metal oxides often contain more impurities/defects, and have generally degraded properties relative to vapor-deposited films, which is a current limitation. However, significant progress has been made over the past decade to enable the production of solution-processed metal-oxide thin films of high (opto)electronic quality competitive with vacuum-deposited films.[7,28,29] These advances have been aided by enhanced understanding of how the solution-precursor chemistry effects the structure/morphology (grain size, density, degree of

condensation, etc.) of resulting thin-film materials, which directly influences their function. Such relationships are well-established for films prepared from sol-gel precursors.[30,31] However, significant knowledge gaps remain in the understanding of the chemical reaction pathways from metal-salt precursors to metal-oxide films which, in many cases, produce higher-quality films (i.e. denser, fewer impurities, etc.) than sol-gel precursors.[32,33] Here we discuss how the chemical transformations of metal-nitrate solution precursors influence metal-oxide film formation chemistry and resulting film properties through an analysis of the solid-state bulk, solution, and thin-film literature.

Among salt precursors for metal-oxide films, metal nitrates, $M(NO_3)_x$, have proved superior to other commonly used precursors (e.g. metal chlorides and acetates). Films produced from metal nitrates are generally denser, contain fewer impurities, and require lower processing temperatures due to the volatility of their decomposition byproducts.[33,34] Consequently, the resulting thin films often exhibit excellent electronic properties for solution-processed films, and have been implemented as semiconductors,[32,35–38] dielectrics,[2,37,39–45] transparent conducting oxides (TCOs),[46,47] magnets,[48] solid electrolytes,[49] and charge-carrier selective contacts.[50,51] Nitrate counterions exhibit unique reactivities that make them susceptible to decomposition pathways involving little to no thermal annealing. Such "low-temperature processing" methods, including combustion synthesis,[52] ultraviolet (UV) photolysis,[53] and humid-atmosphere annealing,[54] have been investigated for thin-film processing in efforts to improve compatibility with low-melting point polymeric substrates and enable roll-to-roll processing.[2,29,55,56]

While the use of metal-nitrate precursors has become ubiquitous, a fundamental understanding of the nitrate decomposition pathways and the oxide-formation processes is important for the advancement of thin-film solution-deposition technologies. This review examines the important chemical considerations that enable the preparation of high-quality metal-oxide thin films from metal-nitrate precursors. An improved understanding of metal-nitrate chemistry, including the thermal evolution and decomposition of bulk salts, the chemical nature of metal-nitrate solution precursors, and film-formation reactions in thin-film precursor gels serves to inform process development for metal-oxide thin-film deposition. Such considerations of the entire film reaction pathway, from precursor to metal oxide, provide insights that may facilitate manufacturing of high-quality metal-oxide thin films from metal-nitrate precursors.

2. Metal nitrate-based precursors: chemistry, design, and characterization

2.1 Bulk metal nitrate chemistry

In addition to thin-film precursors, metal-nitrate salts are used for the preparation of bulk metal oxides (and metals) used in numerous materials-science applications. Nitrate salts are preferred to other metal salts due to their relatively low decomposition temperatures and highly-volatile decomposition products, resulting in fewer residual contaminants in the final products.[57] Knowledge of metal-nitrate decomposition mechanisms has proved important for optimizing synthesis conditions to improve material properties. For example, in catalysis, changes to the annealing atmosphere (inert, O_2, H_2, etc.) for metal nitrates can influence metal-oxide-catalyst-particle dispersion,[58] as well as the mechanical and chemical nature of catalyst-support interactions.[59,60] We discuss here chemical factors that influence decomposition behavior of metal nitrates and what implications this has for selecting thin-film precursors and processing conditions to control film-formation reactions.

The mechanism(s) of metal nitrate bulk salt decomposition have been studied extensively by thermogravimetric analysis (TGA).[61–67] Figure 1a shows representative chemical reactions for metal-nitrate salt decomposition in air. Prior to decomposition, the salt melts and releases loosely bound waters (~ 25-75 °C), forming a highly concentrated salt solution. Nitrate can be removed from the salt by two pathways. The first pathway (Figure 1a, reaction i) involves the removal of some nitrates via nitric acid (HNO_3) formation and the subsequent evaporation of the water-acid azeotrope (68% HNO_3/ 32% H_2O), which boils at 120 °C. At higher annealing temperatures (~ 200-500 °C, depending on the metal-cation identity), remaining nitrate thermally decomposes to NO_x gases (Figure 1a, reaction ii).[57,68] The nitrate thermal decomposition pathway is complex, with many possible NO_x decomposition products (NO, NO_2, N_2O, N_2O_2, etc.).[68] The distribution of products varies with the metal identity and temperature. Thermal decomposition at lower temperatures typically involves formation of NO, NO_2 and N_2O; as the temperature is increased, NO and O_2 become the primary decomposition products.[68] This general description of the nitrate decomposition pathway also applies to thin films (see *3.2 Characterization of the metal oxide thin film reaction pathway*). Following nitrate decomposition, the resulting solid metal-hydroxide product then condenses to form the final metal oxide (Figure 1a, reaction iii). These reactions are often concurrent, resulting in overlapping mass loss events in TGA, which makes full characterization of the metal-nitrate decomposition reactions challenging.

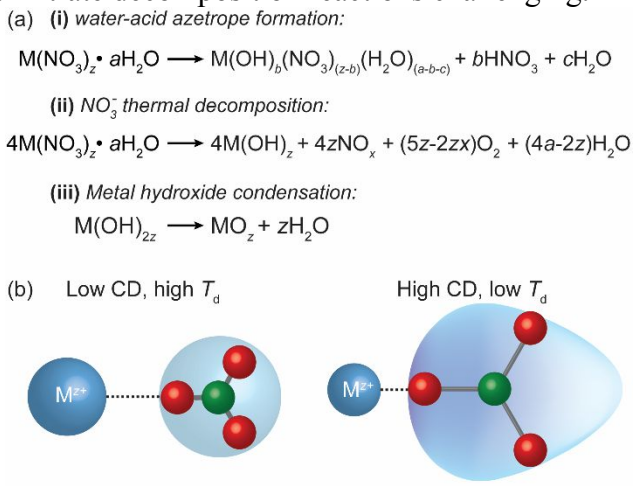

Figure 1. Bulk metal nitrate decomposition. (a) Representative chemical reactions for metal-nitrate-hydrate thermal decomposition in air. (b) Schematic depicting the electronic interaction between M^{z+} and nitrate. Low charge-density (CD) metals are unable to polarize the nitrate electron cloud, resulting in high T_d (left), whereas high-CD metals attract the electron density of nitrate (indicated by distortion and shading of the electron cloud), which lowers T_d (right).

Metal-nitrate salts have a wide range of decomposition temperatures due to differing electronic interactions between the metal and nitrate.[57] Positively-charged cations polarize the electron cloud of the negatively-charged nitrates. This lowers the N-O bond order (i.e. lengthens and weakens the bonds), which promotes nitrate dissociation and decomposition. For metals with accessible *d* orbital vacancies, π-back donation of nitrate electron density can occur, which further lowers the N-O bond order. The metal-ion charge density (CD) is a measure of its polarizing ability ($CD = \frac{3z}{4\pi r^3}$, where z = atomic charge and r = atomic radius in nm), which dictates the covalent nature of the metal and nitrate interaction. Yuvaraj et al. studied the decomposition behavior of alkali, alkaline-earth, main-group, and transition-metal nitrates,[57] and observed an inverse correlation between metal-cation CD and the nitrate-salt decomposition temperature (T_d).[57] Low-CD cations have little

influence on the nitrate electron cloud and T_d tends to be high (Figure 1b, left). High-CD cations effectively polarize nitrates, which facilitates decomposition and lowers T_d (Figure 1b, right).

We have studied the decomposition behavior of a broad selection of hydrated metal-nitrate salts that are relevant to solution deposition, including rare-earth lanthanides (Ln), which have recently gained popularity as precursors for LnO_x gate dielectrics.[39,40,69,70] TGA curves for these metal-nitrate salts are shown in Figure 2. We define T_d as the temperature at which the metal-nitrate salt has lost 75% of its total volatile mass.[71] For the metal-nitrate hydrate salts considered here, the inverse correlation between CD and T_d that Yuvaraj previously established generally holds (Figure 3 and Table 1). For the lanthanides, which all have similar CDs, we do not observe an obvious trend in T_d. The mechanism behind the experimentally observed trends in T_d for lanthanides appears to be missing from the literature.

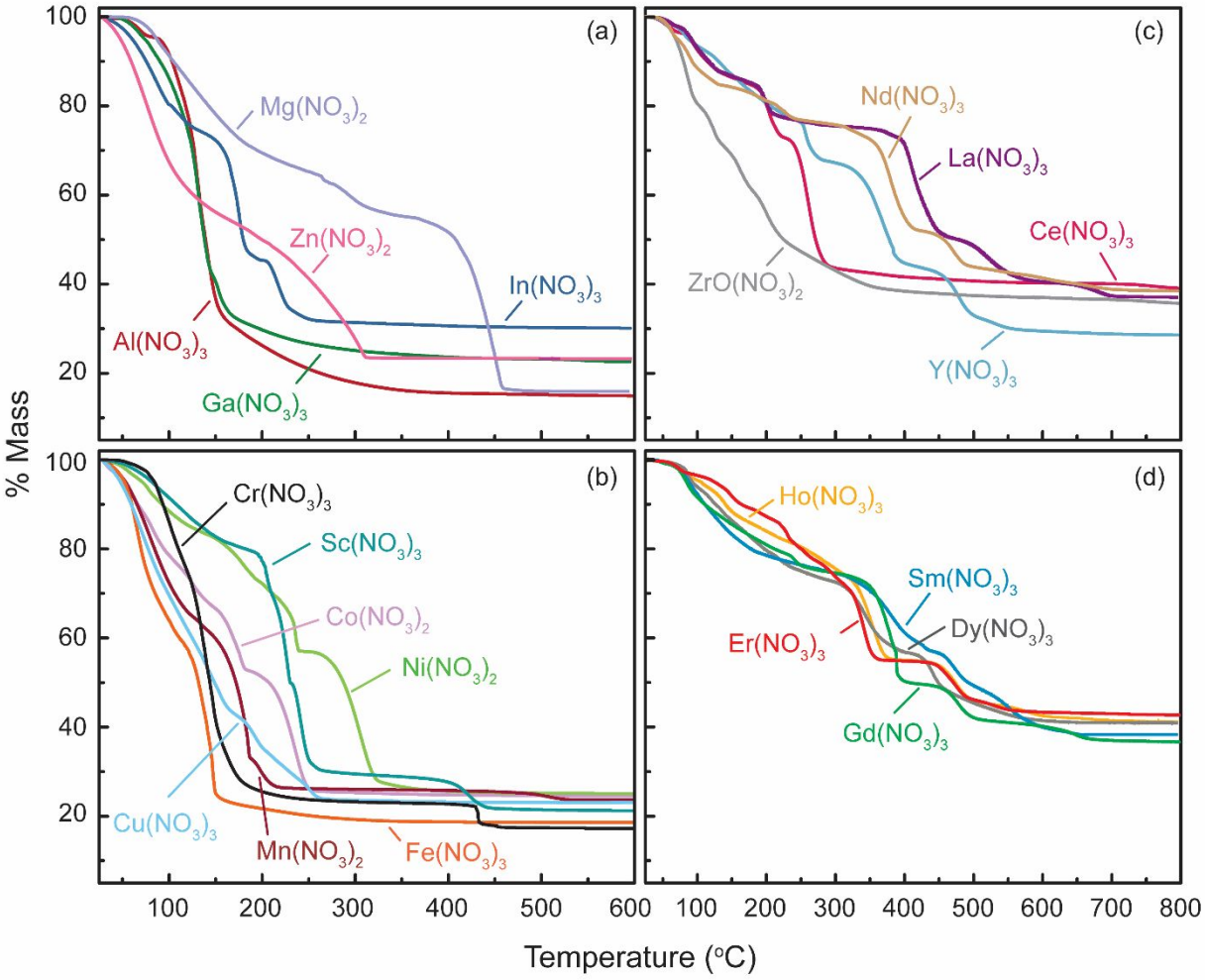

Figure 2. Thermogravimetric analysis (TGA) of metal nitrates used as solution precursors. TGA curves are shown for hydrated metal nitrate salts of: (a) main-group metals, (b) first-row transition metals, and (c) and (d) lanthanide(-like) metals. Experimental details can be found in Ref. 72.

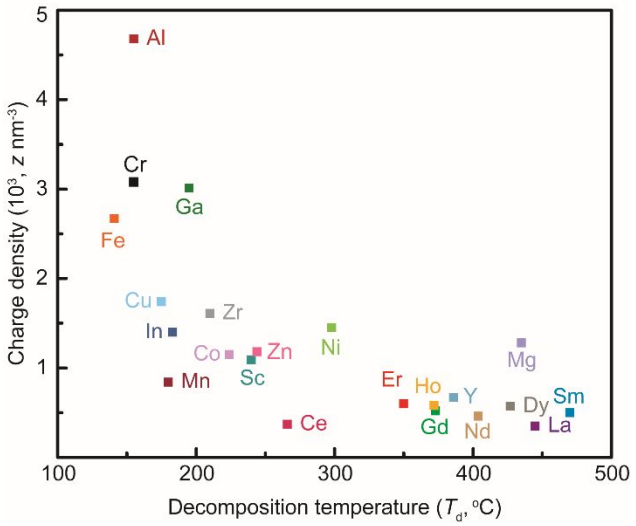

Figure 3. Metal-nitrate decomposition temperature (T_d) as a function of metal-cation charge density (CD). Metal-nitrate salts exhibit a broad range of decomposition temperatures due to electronic interactions between the metal and nitrate. As a general trend, T_d increases with decreasing CD (i.e. the cation polarizing ability decreases). T_d is defined as the temperature at which the salt has lost 75% of its volatile mass.

Table 1. Summary of metal-ion parameters relevant to calculating charge density and thermal-decomposition temperature (T_d). Coordination numbers (CN) and ionic radii are determined based on the coordination and valence state of the metal in their respective hydrated metal-nitrate salts.

Cation (M^{z+})	T_d (°C)	CN[ref]	ionic radius (pm)[73]	CD (10^3 z nm^{-3})
Mg^{2+}	435	6[74]	72	1.28
Al^{3+}	155	6[75]	53.5	4.68
Ga^{3+}	195	6[76]	62	3.01
In^{3+}	183	6[77a]	80	1.40
Sc^{3+}	240	8[78]	87	1.09
Cr^{3+}	155	6[79]	61.5	3.08
Mn^{2+}	180	6[80]	83	0.84
Fe^{3+}	141	6[81]	64.5	2.67
Co^{2+}	224	6[82]	74.5	1.15
Ni^{2+}	298	6[83]	69	1.45
Cu^{2+}	175	5[84]	65	1.74
Zn^{2+}	244	6[85]	74	1.18
Y^{3+}	386	8[86]	102	0.67
Zr^{4+}	210	8[87]	84	1.61
La^{3+}	445	10[88]	127	0.35
Ce^{3+}	266	10[89]	125	0.37
Nd^{3+}	404	9[90]	116	0.46
Sm^{3+}	470	10[91b]	113	0.50
Gd^{3+}	373	9[92]	111	0.52
Dy^{3+}	427	9[93]	108	0.57

Ho^{3+}	372	9[94]	107	0.58
Er^{3+}	350	9[c]	106	0.60

[a] $In(NO_3)_3$ crystal structure reports CN = 7. Radius for CN = 6 (as reported in Ref. 77) is used for this CD calculation.

[b] $Sm(NO_3)_3$ crystal structure shows CN = 10. Radius for CN = 9 (as reported in Ref. 73) is used for this CD calculation.

[c] Crystal structure for $Er(NO_3)_3$ is not reported. Assumed CN = 9 due to similarity to other lanthanides.

In addition to the metal identity, nitrate decomposition is sensitive to the annealing ambient. Yuvaraj et al. also investigate metal-nitrate decomposition temperatures in reducing atmospheres (T_r) of 10% H_2 in N_2.[57] They observe $T_d < T_r$ for many first-row transition and group 13 metal nitrates, whereas many of the alkali, alkaline-earth, and noble-metal nitrates exhibit $T_d > T_r$. This difference in reactivity is explained by the ability of the lower-CD metals (i.e. alkalis, alkaline earths, and noble metals) to adsorb and dissociate H_2, forming NH_3 (or even N_2) and H_2O as byproducts. The authors propose that the (post-)transition metals, in contrast, do not undergo nitrate reduction by this pathway due to ineffective polarization and dissociation of H_2, due to the covalent nature of metal nitrate interactions. Low-CD metals, in contrast, experience mostly ionic metal-nitrate interactions and, therefore, can more effectively dissociate H_2.

While additional systematic studies on this effect are lacking, select examples of other annealing atmospheres influencing T_d exist in the literature. Water vapor is observed to lower T_d for some metal-nitrate systems, including $La(NO_3)_3$,[95] $Mn(NO_3)_2$,[67] and a nitrate-ligated scandium dimer species.[96] This effect has been attributed to suppression of metal-carbonate intermediate species,[95] which decompose at higher temperatures than nitrates, as well as enhanced nitrate removal via HNO_3-H_2O azeotrope evaporation.[96] When NO is introduced to the annealing atmosphere for $Ni(NO_3)_2$ and $Co(NO_3)_2$, the decomposition rate slows compared to a pure O_2 atmosphere, resulting in improved NiO and Co_3O_4 nanoparticle size dispersity.[97] Support materials can also influence decomposition. Alumina supports have been shown to lower T_d for first-row transition-metal nitrates with *d* occupations other than d^5 and d^{10} (e.g. Ni^{2+}, Co^{2+}, and Cu^{2+}) compared to the bulk; the authors hypothesize that alumina changes the metal-nitrate electronic structure, thereby facilitating decomposition.[98]

Metal-nitrate T_d is primarily dictated by the metal-cation identity (i.e. charge density/ electrostatic interaction with nitrate), but is also influenced by ambient conditions (discussed above). For applications where metal-nitrate precursor solutions are employed to deposit metal-oxide films, the metal-nitrate T_d is an important consideration for compatibility with substrates and other device components. In some cases, compatibility may limit the choice of metal-nitrate salts. For example, the high T_d of $Y(NO_3)_3$ and $La(NO_3)_3$ in air (386 and 445 °C, respectively) render them unsuitable as a dielectric layer for flexible TFTs on a polyimide substrate, which softens and deforms above 275 °C.[55] Suitable alternatives would include $Al(NO_3)_3$ or $Ga(NO_3)_3$, as these salts are substantially decomposed by 150 °C (Figure 2). In other cases, a particular metal-oxide target may be critical for a desired application. In this instance, strategies to alter the T_d by controlling the ambient annealing atmosphere or composition may be possible. Our research groups have demonstrated enhanced nitrate removal at low annealing temperatures for Y- and La-based thin films using a water vapor atmosphere (see *3.3.3 Controlled-atmosphere annealing: the role of water vapor in film formation*).[54] Additionally, pairing high-T_d salts, like $La(NO_3)_3$, with low-T_d salts (e.g. $Al(NO_3)_3$ or $ZrO(NO_3)_2$) in ternary oxide compositions effectively lowers the overall T_d of the thin-film system.[39,42,99] We hypothesize this effect is a result of high-CD cations polarizing nitrate ions from the low-CD salt, facilitating their decomposition. Indeed, the process parameter

space to influence metal-nitrate decomposition chemistry is expansive. Further investigation of factors influencing nitrate T_d could allow for improved control over thermal processing conditions and thus the final film properties/performance.

2.2 Aqueous solution behavior of metal nitrates

Metal nitrate salts are highly soluble in aqueous and (polar) organic solvents. Upon dissolution, complex equilibria and speciation are established, the details of which are generally not well understood. Even in dilute salt solutions ($\geq 10^{-4}$ M M^{z+}), monomeric cations can react to form polynuclear species, which can be present in equal concentrations to monomer, depending on solution conditions.[100] At concentrations relevant to solution processing, ($\geq$ 0.1 M M^{z+}) metal-anion complexes can form, further complicating solution speciation.[101–103] Both oligomerization and complex formation depend on pH, concentration, and temperature. Understanding the chemical speciation and interactions taking place in solution can inform precursor design, allowing for control of decomposition pathways and the production of thin films with desired morphology and structure. Examples of speciation-informed precursor design will be highlighted in section *2.3 Tuning metal-nitrate precursor chemistry*. For simplicity, we focus the solution-speciation discussion here on aqueous metal nitrates; however, many of the concepts discussed are also relevant to any solvent system that includes water as a component (e.g. alcohol/water mixtures), including those used in traditional sol-gel chemistry.[30]

2.2.1 Metal ions in solution

When dissolved in water, positively-charged cations (M^{z+}) experience an electrostatic attraction towards the lone electron pairs on oxygen in water to form an ordered hydration shell around M^{z+} – this is referred to as an aquo (or aqua) cation. The electron lone pairs on water molecules in the aquo cation are attracted to the positively-charged M^{z+} and form a strong M-O interaction. Electron density from O-H moves closer to oxygen in order to compensate for lost electron density that is now shared with M^{z+}. This results in an increased partial positive charge on hydrogen. If the electrostatic attraction between M^{z+} and oxygen is strong enough, the positive charge on hydrogen will increasingly resemble H^+, eventually resulting in hydrolysis and the dissociation of H^+ into solution (eq. 1).

$$\left[\mathrm{M(H_2O)}_N\right]^{z+} + h\mathrm{H_2O} \leftrightarrow \left[\mathrm{M(OH)}_h\mathrm{(H_2O)}_{N-h}\right]^{(z-h)+} + h\mathrm{H_3O^+} \quad (1)$$

Such hydrolysis reactions are the origin of metal-cation acidity. Relative cation acidities can be determined from their pK_a values. Metals with pK_a values $\leq$ 6 are considered to be acidic, whereas those with pK_a values > 6 are said to be weakly acidic to nonacidic.[104]

The presence of hydroxyl ligands makes possible the formation of soluble, polynuclear cationic species through condensation reactions. Two condensation pathways are possible: olation and oxolation. Olation occurs via nucleophilic attack of an M-OH group on another metal aquo cation to form a bridging hydroxyl ligand; water is the leaving group (eq. 2).

$$\mathrm{M-OH + M-H_2O \rightarrow M-OH-M + H_2O} \quad (2)$$

Oxolation results in metal oxo linkages (M-O-M) when two OH ligands react and form water as a byproduct (eq. 3).

$$\mathrm{M-OH + M-OH \rightarrow M-O-M + H_2O} \quad (3)$$

The kinetics of olation are rapid compared to oxolation.[100] Therefore, oxolation will not occur to an appreciable extent until H_2O ligands have been eliminated by olation.[105] Soluble oxolation products are most common for highly-charged cations ($z \geq 4$), as these cations have high h:M^{z+} ratios (see eq. 1) due to low (or even negative) pKa values (i.e. few H_2O ligands are present).[104,106] Oxolation reactions of low-valence cations ($z \leq 4$) often results in the precipitation of hydroxides/oxyhydroxides. Because most metal-nitrate salts are low-valence ($z = 2$ and 3), olation products are more commonly observed in metal nitrate solutions.

Olation products with discrete stoichiometry form due to self-limiting reactivity. Olation kinetics are limited by the lability of H_2O ligands, which is quantified by the water-exchange rate constant (k_{H_2O}, s^{-1}). The k_{H_2O} is defined as the equilibrium psueodo-first-order rate constant at which water molecules in the inner-most solvation sphere of the metal cation are exchanged with "bulk" water molecules from solution at 25 °C (i.e. $[M(H_2O)_6]^{z+} + H_2O^* \overset{k_{H_2O}}{\leftrightarrow} [M(H_2O)_5(H_2O^*)]^{z+} + H_2O$; $\text{rate} = k_{H_2O}\left(c_{[M(H_2O)_6]^{z+}}\right)$ where c is the concentration).[107] As a general trend, k_{H_2O} for metal cations increases with increasing ionic radius (see Figure 6c). For *d*-block metals with partially-occupied *d* states, the ligand-field stabilization energy (LFSE) also influences the strength and lability of M-H_2O bonds. Cations with higher LFSE experience slower k_{H_2O} as a result of greater orbital overlap between metal *d* orbitals and those of H_2O.[107] Additionally, OH ligands must be good nucleophiles in order for olation to occur. The OH ligands on metal olation products become less nucleophilic (i.e. δ(OH) becomes less negative) as they form more bonds and the positive charge on the polynuclear species increases, which slows k_{H_2O}.[100] This leads to the formation of polynuclear species with a defined stoichiometry, rather than indefinite oligomerization. For many metal cations, olation stops at or before hexamer formation,[108] although some cations are capable of forming larger polycations. The OH bridges in small olation products, such as trimers, can remain good nucleophiles and further react to form large clusters. Such is the case for Al^{3+}, which forms the tridecameric Keggin ion $[Al_{13}O_4(OH)_{24}(H_2O)_{12}]^{7+}$ under certain pH and concentration conditions.[105]

Solution equilibria and the existence of polynuclear species, which can include multiple hydrolysis products, can be complex and challenging to predict. Pourbaix diagrams are helpful representations that depict predominant species in solution under equilibrium as a function of pH and concentration.[109] We consider here the Pourbaix diagrams of two commonly-used metal systems in solution processing: aluminum and indium. For an aqueous solution with 0.1 M metal ion concentration, the monomeric trivalent aquo ions Al^{3+} and In^{3+} are the predominant species up to pH ~ 3.7 and ~ 2.8, respectively, after which $M(OH)_3$ persists (Figure 4a-b). Thin-film precursor solutions should be maintained at a pH below that at which insoluble $M(OH)_3$ forms, as this can result in material loss and/or negatively affect film morphology. Additionally, excess acid is typically detrimental to film quality given that additional volatile components must be removed during densification, which can lead to increased porosity. While Pourbaix diagrams are useful for determining the predominant species under equilibrium conditions, they leave out hydrolysis/olation products that may contribute appreciably to soluble species in solution. For a more-complete depiction of solution speciation, we must consider speciation diagrams.

Speciation diagrams describe the evolution of solution equilibria as a function of pH. These diagrams are calculated from thermodynamic values and describe the distribution of soluble species in equilibrium with the solid $M(OH)_x$ phase. Baes and Mesmer compiled a library of

equilibrium constants for polynuclear hydrolysis products used to formulate such speciation diagrams.[108] For a 0.1 M Al^{3+} solution, monomeric Al^{3+} (or $Al(H_2O)_6^{3+}$) persists as the dominant ionic species up to pH 3.5 (Figure 4c). As pH increases above pH 3, the concentration of $Al_{13}O_4(OH)_{24}^{7+}$ (the "Al_{13}" Keggin ion) increases to ~35% of soluble Al species near the precipitation boundary (pH 3.7). Minor hydrolysis products $Al(OH)^{2+}$, $Al_2(OH)_2^{4+}$, and $Al_3(OH)_4^{5+}$ have narrow stability windows centered around pH 3.5 and, combined, contribute less than 10% of soluble species at pH 3.5 (Figure 4c). For a 0.1 M In^{3+} aqueous solution, In^{3+} (or $In(H_2O)_6^{3+}$) is the predominant species below pH 2. As solution pH increases from ~1 to 2, the hydrolysis product $In_3(OH)_4^{5+}$ increasingly contributes to solution speciation up to 50% at pH 2 (Figure 4d). Soluble species at pH values above the hydroxide precipitation boundary, indicated by the unshaded region in Figure 4b and 4c, are not relevant when considering thin-film solution precursors due to low solubilities.

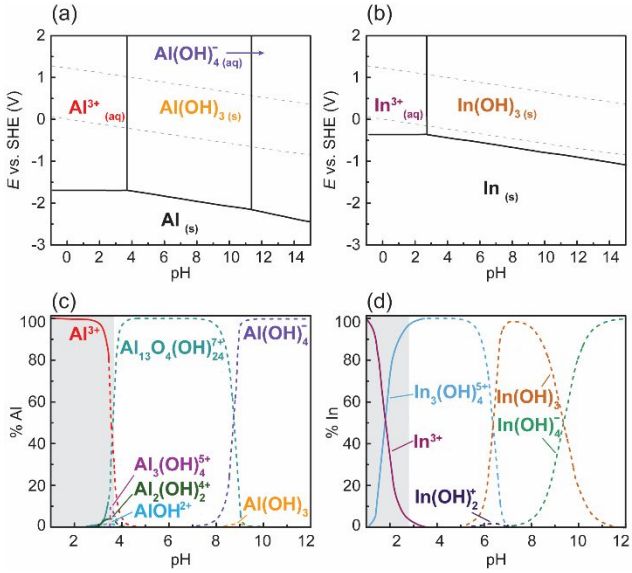

Figure 4. Solution speciation of aluminum and indium. Pourbaix (a-b) and speciation (c-d) diagrams describing the aqueous chemistry of aluminum and indium. The dashed lines in panels c and d indicate species in solutions super-saturated with respect to α-$Al(OH)_3$ and $In(OH)_3$ (i.e. $M^{z+} < 0.1$ M). Grey shading in panels c and d indicates the region to the left of the $M^{3+}|M(OH)_3$ boundary from the Pourbaix diagram (i.e. the pH region where soluble species predominate). The data used to construct the Pourbaix and speciation diagrams are from Ref. 110 and 108, respectively.

Baes and Mesmer's publication, "The Hydrolysis of Cations," is still considered the most-comprehensive treatment of solution speciation; however, Baes and Mesmer acknowledge their published solution speciation diagrams are far from complete.[108] Identifying and characterizing polynuclear species is a difficult task and is, indeed, an active area of research. Significant progress toward solution speciation characterization has been made in recent years with the aid of a suite of corroborative techniques, including nuclear-magnetic-resonance (NMR) spectroscopy, dynamic light scattering (DLS), and small-angle x-ray scattering (SAXS).[111] In the field of Al speciation, our research groups have prepared and studied $[Al_{13}(OH)_{24}(H_2O)_{24}]^{15+}$ ("flat"-Al_{13}) and $[Al_8(OH)_{14}(H_2O)_{18}]^{10+}$,[112,113] while others have previously observed $[Al_{30}O_8(OH)_{56}(H_2O)_{24}]^{18+}$ in aqueous solution.[114] Additional indium hydrolysis products ($In_2(OH)_2^{4+}$ and $In_4(OH)_6^{6+}$) have also been experimentally identified.[115] Recent computational work on Al and Ga speciation predicted some polynuclear species are predominant, thermodynamic products that belong on Pourbaix

diagrams.[116] It is important to note that the identity of the counterion can also influence speciation if it is capable of coordination to the metal,[117] which can, in turn, influence the identity and quantity of olation products. Additionally, metastable polynuclear products can become kinetically trapped due to stabilizing effects from counterions.

There are numerous approaches to systematically influence thin-film precursor solution speciation by changing solution pH. Perhaps the most straightforward approach involves controlling the metal salt concentration, which will necessarily change the pH and the olation product distribution. For a constant metal concentration, solution pH can be controlled using acid or base addition. Dissolution of metal oxides/hydroxides using HNO_3 has proven a successful approach for targeting olation products of interest as thin-film precursors.[47,118] However, the addition of excess acid or base to solution should be avoided, as such additives can have a deleterious effect on film morphology, imparting porosity and inhibiting densification. Alternatively, redox reactions that consume protons and nitrate can be used to increase the solution pH and drive olation. This can be accomplished via electrochemical reduction to avoid introducing additives.[119] For mixed-metal precursors, the effect of the component metal cations on the solution pH must also be considered. We have observed the formation of olation products in mixed Al^{3+} and La^{3+} nitrate precursors.[39] Because La^{3+} is less acidic than Al^{3+} (pK_a = 7.6 and 5.0, respectively),[104] La^{3+} increases the solution pH, which drives the formation of Al clusters. These approaches are discussed in more detail in section *2.3.1 Olation products as thin-film precursors*. An understanding of the solution-speciation chemistry for thin-film precursors is useful for relating solution conditions to thin-film chemistry and morphology, which influences their performance in devices.

2.2.2 Nitrates in solution

Nitrates do not exhibit the same complex speciation chemistry as metal cations, but can be (electro)chemically reduced to a variety of nitrogen-containing species in aqueous solution. The nitrogen Pourbaix diagram shows the predominant (soluble) reduction products for nitrate as a function of pH and solution potential (E) (Figure 5). For metal-nitrate solutions, which are typically acidic (pH < 7), NH_4^+(aq) is the predominant thermodynamic reduction product in solution at E < 0.86 V. From $E \approx$ 0.1-1 V, HNO_2 (aq) and NO_2 (aq) have narrow predominance regions at pH < 3 and from pH = 3-7, respectively. While other nitrate-reduction products are possible, including N_2, NO, N_2O, and N_2O_5, these products are gases of low solubility.[109,110] In section *2.3.1 Olation products as thin-film precursors*, we discuss the importance of metal-nitrate reduction chemistry in the design and control of thin-film precursor solution speciation.

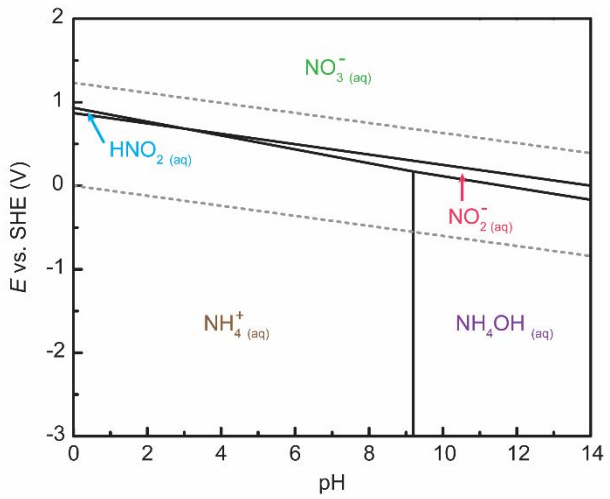

Figure 5. Nitrate reduction chemistry. The above Pourbaix diagram shows the aqueous solution speciation of nitrogen (0.1 M). The aqueous stability of nitrate is pertinent to understanding its reduction chemistry, which can be utilized to influence metal-nitrate precursor solution speciation. The data used to construct this Pourbaix diagram is from Ref. 110.

In addition to considering metal cation and nitrate solution chemistry independently, it is important to understand how these species interact in solution. Metal-anion complexes form in aqueous solutions under certain concentration conditions.[101–103,120,121] Metal-nitrato complexes (i.e. $[M(NO_3)(H_2O)_{N-1}]^{(z-1)+}$, abbreviated here as "M-NO_3") have been identified and quantified using Raman spectroscopy. For $In(NO_3)_3$, In-NO_3 complex can be identified by a shift in the InO_6 vibrational mode, and appearance of additional vibrational modes, as $In(NO_3)_3$ concentration is increased (Figure 6a).[101] Changes to the Raman spectra result from broken symmetry of the aquo cation ($[In(H_2O)_6]^{3+}$) when nitrate substitutes for a water molecule to form In-NO_3. The following quantities of M-NO_3 complex (compared to the amount of $[M(H_2O)_N]^{z+}$) for a select few metal cation systems relevant to thin-film solution precursors are as follows: In^{3+}(60%)[101] > Y^{3+}(45%)[102] ≈ La^{3+} (44%)[103] > Ga^{3+}(5%)[121] > Al^{3+}(0%)[120] (~ 2 M [M^{3+}] in aqueous solution). For all metal cations, the quantity of M-NO_3 complex decreases with decreasing [M^{z+}] and [NO_3^-].

The dependence of M-NO_3 complex formation on metal cation identity can be explained by considering the relative thermodynamic stabilities of the aquo cations and the M-NO_3 complex. The free energy of hydration (ΔG_{hyd} for the reaction: $M^{z+}(g) + nH_2O(l) \rightarrow M^{z+}(aq)$) provides a measure of the thermodynamic stability of hydrated metal cations. ΔG_{hyd} for the cations considered here are as follows: -4525 kJ mol^{-1} (Al^{3+}) < -4515 kJ mol^{-1} (Ga^{3+}) < -3980 (In^{3+}) < -3450 (Y^{3+}) < -3145 kJ mol^{-1} (La^{3+}).[122] Al^{3+} and Ga^{3+} form stable aquo cations (i.e. large, negative ΔG_{hyd}), due to their high charge densities, which result in strong M-H_2O bonds; this may explain why little to no M-NO_3 complex is observed for Al^{3+} and Ga^{3+}. In contrast, $In(NO_3)_3$ forms the largest quantity of M-NO_3 complex. The stability constant (K_1) for In-NO_3 (0.18) is also larger as compared to La-NO_3 (0.1), despite the trend in ΔG_{hyd}. The reaction described by K_1 is given in eqn. 4. The fact that In-NO_3 is more stable than La-NO_3 is likely related to an optimal binding interaction between indium and nitrate due to cation size, charge density, and/or possibly differences in nitrate binding mode (e.g. monodentate vs. bidentate). Significant gaps in published K_1 values for M-NO_3 prevent us from making thorough comparisons of M-NO_3 stabilities.

$$[\mathrm{M(H_2O)}_N]^{z+} + \mathrm{NO_3^-} \leftrightarrow [\mathrm{M(NO_3)(H_2O)}_{N-1}]^{(z-1)+} + \mathrm{H_2O} \quad (4)$$

Consideration of thermodynamic and kinetic parameters of aquo cations can be useful for predicting if M-NO_3 may form, if K_1 data is not available. The ΔG_{hyd} exhibits a linear relationship with cation size (r) (Figure 5b). Deviations from this trend arise for some first-row transition metal cations; weak ligand-field effects make filling of the anti-bonding e_g orbitals favorable, resulting in an expansion of the cation radius that weakens M-H_2O bonds (i.e. ΔG_{hyd} values are lower than predictions based on r).[107] To first approximation, strongly-hydrated cations (i.e. large, negative ΔG_{hyd}) are expected to be thermodynamically stable and will likely form lower equilibrium concentrations of M-NO_3. It is also important to know the timescale required to establish equilibrium concentrations of the M-NO_3 complex (eqn. 4). This can be determined by considering the water exchange rate (k_{H_2O}). k_{H_2O} values tend to increase with increasing r but level off for $r >$ 80 pm as a result of weakening M-H_2O bond strengths (Figure 5c). The k_{H_2O} for the cations reported here suggest equilibrium for most aqueous metal nitrate solution is established in a matter of seconds.[107] The exception, Cr^{3+}, requires several days to reach equilibrium, as the exchange reaction requires the formation of a high-energy transition state.[123] In section *2.3.2 Mitigating metal-nitrato (M-NO_3) complex formation in solution*, we will discuss ways in which M-NO_3 complexes in thin-film precursor solutions influence the thin-film reaction pathway and the final metal-oxide thin-film properties.

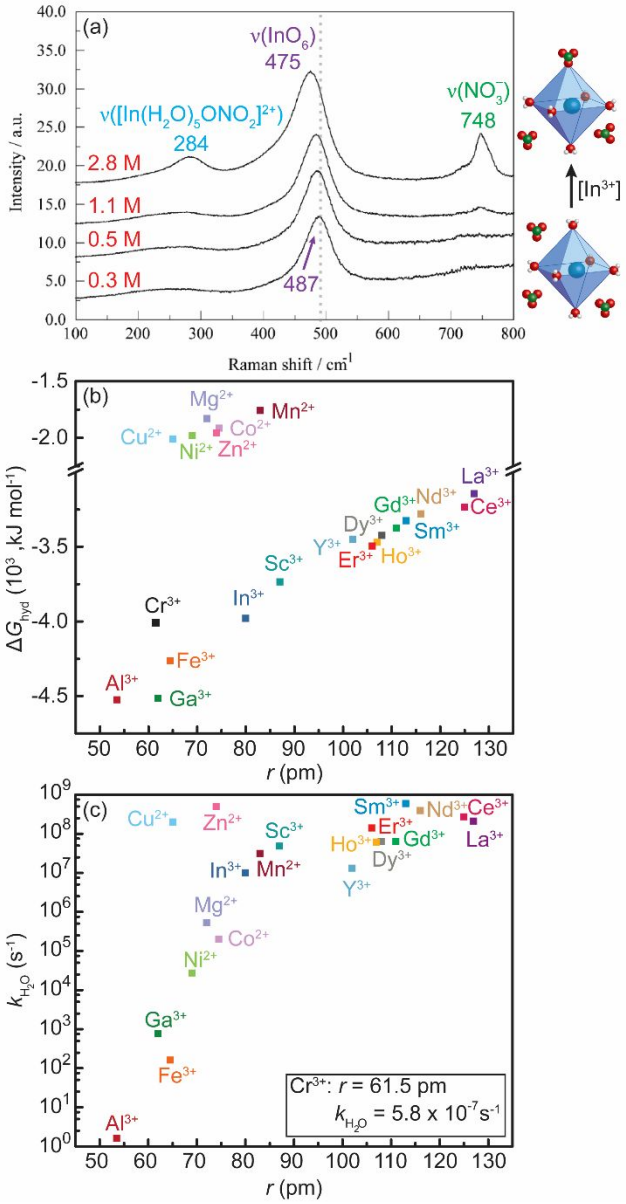

Figure 6. Metal-nitrato (M-NO_3) complex formation. (a) Raman spectra of $In(NO_3)_3$ solutions. Raman frequencies shift and new vibrational modes appear as $[In^{3+}]$ increases, indicating M-NO_3 complex formation. The figure is adapted from Ref. 101 with permission from the PCCP Owner Societies. (b) Relationship between cation radius (r) and ΔG_{hyd} (values from Ref. 122). Cations that are more strongly hydrated (i.e. more negative ΔG_{hyd}) are thermodynamically stable and tend to form fewer M-NO_3 complexes. Deviation of z = +2 first-row transition metals from this trend is due to weak ligand-field effects, which results in cation radius expansion when e_g orbitals are filled.[107] (c) Relationship between cation radius (r) and k_{H_2O}. Exchange kinetics will dictate how quickly equilibrium concentrations of M-NO_3 complex will be established in aqueous solution. Values are complied from Ref. 101,124,125.

2.3 Tuning metal nitrate precursor chemistry

While metal-salt solution speciation is complex, some control can be achieved by altering solution pH, concentration, and/or temperature. Changing these parameters influences olation and metal-anion-complex equilibria. Here we discuss strategies to control metal-nitrate solution

speciation for thin-film precursor design. We highlight examples that demonstrate how solution speciation influences thin-film morphology, chemical composition, and function.

2.3.1 Olation products as thin-film precursors

Our research groups (among others) have a history of developing scalable synthetic methods for olation products, specifically nitrate-stabilized metal hydroxo nanoclusters, for use as thin-film precursors. Such nanoclusters were targeted to solve common challenges associated with traditional sol-gel precursors for film deposition. In sol-gel syntheses, pre-condensation reactions are initiated in solution to control film morphology and ensure atomic-level mixing in multi-metal systems.[126] Organic solvents and additives are critical for controlling hydrolysis and condensation reactions in sol-gel chemistry. Solution equilibria can be shifted in order to influence the sol-gel precursor structure to alter reactivity and selectivity toward hydrolysis and condensation. This can be accomplished by controlling metal-ligand binding strengths, changing metal/ligand ratios, and/or the addition of acid or base catalysts. See Danks et al. for a detailed review of the chemical reactions/interactions relevant to sol-gel formation.[126] Removal of these organic species during thermal processing can negatively influence film morphology through cracking and/or the incorporation of pores.[30,127–129] In contrast, nanoclusters are pre-condensed with networks of hydroxyl linkages, and can be thought of as an "all-inorganic" analog to sol-gel thin-film precursors, as these nanoclusters typically contain inorganic anions for charge balance instead of organic ligands. The presence of a pre-condensed metal-hydroxo network and the lack of organic solvents or ligands allows nanoclusters to densify more readily, resulting in films with fewer morphological defects. Indeed, this pre-condensed metal-hydroxyl network should also prevent crystallization of monomer salts during solvent evaporation, resulting in homogeneous film morphology. Additionally, heterometallic nanoclusters inhibit phase segregation during film formation to achieve uniform distribution of mixed-metal compositions.

Two classes of nitrate-stabilized metal-hydroxo nanoclusters commonly utilized as thin-film precursors have the general formula $[M_{13}(OH)_{24}(H_2O)_{24}](NO_3)_{15}$ (i.e., "M_{13}" where M can be Al^{3+} or Ga^{3+})[112,119,130–135] or $[Ln_6(O)(OH)_8(H_2O)_{12}(NO_3)_6](NO_3)_2$ (i.e., "Ln_6", where Ln = Y^{3+}, Gd^{3+}, Ho^{3+}, or Er^{3+}).[136] The resulting structure of "M_{13}" nanoclusters has a planar (i.e. "flat") arrangement of octahedrally-coordinated metal sites and "free" nitrate counterions (Figure 7a). A variation of this "M_{13}" cluster type includes substitution of the six exterior metal sites to form heterometallic structures, of which "Ga_7In_6" and "Al_7In_6" have been prepared to date.[112,131]

Olation reactions that lead to nanoclusters of these types are driven by two reactions: proton (eqn. 5) and nitrate (eqn. 6) reduction.

$$H^+ + 2e^- \rightarrow H_2 \ (E^o = 0 \text{ V vs. SHE}) \quad (5)$$

$$NO_3^- + 3H^+ + 2e^- \rightarrow HNO_2 + H_2O \ (E^o = 0.94 \text{ V vs. SHE}) \quad (6)$$

Eq. 5 increases the solution pH, which promotes cation hydrolysis (eqn. 1) and provides the reactive M-OH species for olation (eq. 2). Nitrate reduction (eq. 6), while less thermodynamically favorable than proton reduction, must also occur in order to maintain charge balance as olation products form. Eq. 6 is one of several possible nitrate-reduction reactions, which all have similar reduction potentials (E^o = 0.8 -1 V vs. SHE).[133] These reactions can be initiated with a variety of reductants, including organic molecules (i.e. nitrosobenzene),[130,132] zero-valent metals (Zn or Al),[41,131,134–136] or electrons via bulk electrolysis.[32,119,137] Additionally, such nanoclusters can be

prepared from a "top-down" approach via digestion of metal hydroxide or oxide species in nitric acid. In this way, nanoclusters of a desired stoichiometry, with specific M^{z+}:NO_3 ratios can be targeted. Such "dissolution" methods have thus far been applied to the preparation of flat-"Al_{13}" ($[Al_{13}(OH)_{24}(H_2O)_{24}](NO_3)_{15}$) and tin(II) hydroxide nitrate ($Sn(II)(OH)_x(NO_3)_y$) nanoclusters.[47,118]

There are numerous examples of thin films from "M_{13}" (including its heterometallic variants) and "Ln_6" precursors that have excellent morphology and properties.[32,41,71,112,118,131,136–138] Such films are dense and exhibit essentially atomically-smooth surfaces,[71] which are properties critical for preparing high-performance electronic devices. Here we highlight select studies that demonstrate advances toward addressing common limitations of solution processing by using nanocluster precursors to prepare high-quality films.

As mentioned previously, impurities from solvents and counterions can inhibit condensation and densification processes in solution-deposited metal oxide thin films. To address this challenge, precursors from the "Al_{13}" nanocluster have been used to produce dense, high-quality metal-oxide thin films with excellent insulating properties, as demonstrated in metal-insulator-metal (MIM) diodes. The insulating properties of Al_2O_3 thin films can be directly correlated with the chemical composition as a function of annealing temperature. At low annealing temperatures (350 °C), conduction is dominated by Frenkel-Poole emission at electric fields (ξ) above 3 MV cm^{-1}, which is a trap-mediated conduction mode (Figure 7b, top). The source of these trap states is suggested to be water, nitrate, and hydroxyl impurities remaining in the film, which are detected by temperature-programmed desorption mass spectrometry (TPD-MS) and x-ray photoelectron spectroscopy (XPS). As the film annealing temperature is increased to 600 °C, chemical impurities are increasingly removed. The film further densifies, and, as a result, Frenkel-Poole emission is replaced by Fowler-Nordheim tunneling (Figure 7b, bottom). Fowler-Nordheim conduction requires low-defect density and had only been observed for devices from vapor-deposited thin films prior to this work. This study shows that solution-deposited thin-film properties are sensitive to precursor chemistry and processing conditions. Additionally, having 'precondensed' nanoclusters minimizes the amount of nitrate counterion and water that must be eliminated, aiding condensation and minimizing residual defects in the final films. The high-quality charge-transport characteristics obtained in solution-deposited thin films suggests there is opportunity to further design precursors to expand the application base of solution-processed films to those requiring low-defect-density materials (i.e. flash memory and solar cells).

Nanocluster precursors have also been used to combat phase segregation in multi-metal thin-film systems. Solutions of electrolyzed In-, Ga-, and Zn-nitrate, which contain "Ga_7In_6" with $Zn(NO_3)_2$, can be used to prepare films with a homogeneous distribution of all metal atoms in indium gallium zinc oxide (IGZO) films.[32] In contrast, when the component salts are used ($In(NO_3)_3$, $Ga(NO_3)_3$, and $Zn(NO_3)_2$), In_2O_3 islands decorate the film surface (Figure 7c). Phase segregation appears to be inhibited by the pre-condensed metal-hydroxo network of "Ga_7In_6." Nitrate reduction via electrolysis can also substantially reduces the nitrate concentration in solution, which leads to decreased mass loss during annealing and improved densification of the thin films (20% vs. 50% of the total mass change after a 300 °C anneal). This effect was monitored by thin-film thermal analysis using a quartz-crystal microbalance (QCM; described in *3.2 Thermal annealing to form metal oxide thin films*). Decreased mass loss correlates with denser films, as observed by x-ray reflectivity (XRR). Increased film homogeneity and improved densification translate to improved TFT device performance. Average channel mobilities increase from 5 to 9 $cm^2\ V^{-1}\ s^{-1}$ when electrolyzed solutions are used (followed by a 400 °C anneal). Similar device

performance improvements have been reported for IGO-based TFTs prepared from Ga_7In_6 precursors over films from Ga- and $In(NO_3)_3$ salts.[137]

An alternative strategy to initiate more-complete nitrate removal and condensation involves designing nanoclusters with reducing agents as a functional component of the final metal oxide film. We have synthesized precursors for SnO_2 and F-doped SnO_2 ($F:SnO_2$) that leverage redox reactions between Sn atoms and nitrate in a nanocluster with the general formula $Sn(II)(OH)_x(NO_3)_y$.[47] For F-doped films, SnF_2 is added to solution.

According to the Sn Pourbaix diagram, Sn^{2+} is stable over narrow pH (~ 0-1.6) and potential (~ 0 - 0.25 V) regions within the water stability window,[110] and can oxidize readily to SnO_2 in water (eq. 7). Standard reduction potentials indicate nitrates are capable of facilitating this oxidation process (eq. 8 & 9). The following is one proposed reaction pathway of the nanocluster to SnO_2 (eq. 9).

$$Sn^{2+} + 2H_2O \rightarrow SnO_2 + 4H^+ + 2e^- \quad (E^o = 0.13 \text{ vs. SHE}) \tag{7}$$

$$NO_3^- + 3H^+ + 2e^- \rightarrow HNO_2 + H_2O \quad (E^o = 0.94 \text{ V vs. SHE}) \tag{8}$$

$$Sn^{2+} + NO_3^- + H_2O \rightarrow SnO_2 + HNO_2 + H^+ \quad (E^o_{rxn} = 0.81 \text{ V}) \tag{9}$$

We observed by transmission Fourier transform infrared spectroscopy (FT-IR) that ~ 90% of nitrates are removed after annealing a film from the $Sn(II)(OH)_x(NO_3)_y$ nanocluster precursor at just 100 °C (Figure 7d). We hypothesize the redox reaction shown in eq. 9 facilitates nitrate removal at low temperature. The resulting films are smooth, dense, and amorphous up to a 150 °C annealing temperature; at higher temperatures (e.g. 300 °C) crystalline, nanoporous SnO_2 forms. Porosity is likely caused by rapid, low-temperature metal-oxide network formation, which cannot readily rearrange via solid-state diffusional processes to densify the film. Regardless, the resulting $F:SnO_2$ films are conductive ($\rho < 10^{-2}$ Ω • m at 250 °C annealing temperature) with high optical transparency in the visible spectrum (> 85%). Demonstrated compatibility with polyimide substrates suggest their usefulness as transparent conducting oxide materials for flexible devices.

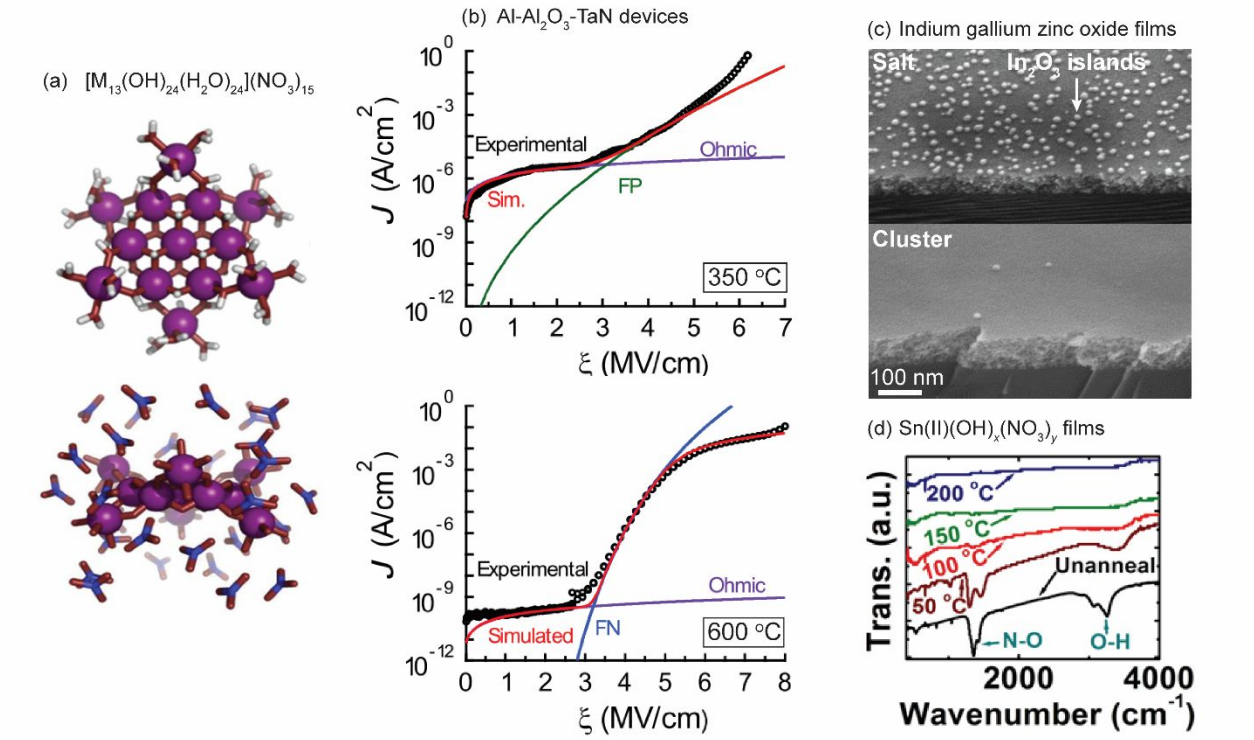

Figure 7. Metal-hydroxo nanoclusters as thin-film precursors. (a) X-ray crystal structure of a $[M_{13}(OH)_{24}(H_2O)_{24}](NO_3)_{15}$ (M = Al^{3+} or Ga^{3+}) with (bottom) and without (top) non-coordinating nitrate counterions. (b) Current (J) – electric field (ξ) curve fitting of conduction mechanisms for Al_2O_3-based devices annealed at 350 (top) and 600 °C (bottom). The 350-°C-annealed film exhibits Frenkel Poole (FP) conduction, whereas the film annealed at 600 °C displays Fowler Nordheim (FN) tunneling. FN tunneling is indicative of a high-quality insulator. Reprinted from Ref. 41. Copyright 2018 American Chemical Society. (c) SEM images of indium gallium zinc oxide (IGZO) films prepared from nitrate salt solutions (top) and electrochemically-treated cluster solutions (bottom). Islands present on the surface of films from the salt precursor are phase-segregated In_2O_3. Electrochemically-treated solutions are believed to inhibit phase segregation as a result of the pre-condensed hydroxo network of "Ga_7In_6.". Images adapted from Ref. 32. Copyright 2015 American Chemical Society. (d) FT-IR spectra of films from the $Sn(II)(OH)_x(NO_3)_y$ nanocluster precursor. Vibrational modes for nitrate and hydroxyl groups (labeled) are nearly undetectable after annealing at 100 °C in air. Reprinted with permission from Ref. 47. Copyright 2013 American Chemical Society.

2.3.2 Mitigating metal-nitrato (M-NO_3) complex formation in solution

At solution concentrations relevant to thin-film precursor solutions (0.1 - 3 M in M^{z+}), many metal salts are capable of forming metal-anion complexes (abbreviated here as M-*X*). The presence of such complexes has been correlated with degraded electronic performance in resulting metal-oxide thin films. Work by Rim et al. on a variety of precursors for In_2O_3 suggests the presence of fully-solvated $[In(H_2O)_6]^{3+}$ ions (i.e. in which there are no metal-anion complexes present) are critical for the preparation of high-quality In_2O_3 thin films at low annealing temperatures.[36] A comparison of the Raman spectra of $In(C_2H_3O_2)_3$, $InCl_3$, InF_3, and $In(NO_3)_3$ aqueous precursor solutions shows evidence of direct metal-ligand bonding in all cases except $In(NO_3)_3$, in which only "free" (i.e. unbound) nitrate is detected ($\nu(NO_3^-)$ = 1050 cm^{-1}) (Figure 8a). A comparison of the stability constants for In-*X* complexes of these salts explains this observation, as the log K_1 value ($[M(H_2O)_6]^{3+} + X^- \overset{K_1}{\leftrightarrow} [M(H_2O)_5X]^{2+} + H_2O$) for $In(NO_3)_3$ complexes is lowest of all the salts investigated, indicating In-NO_3 complexes are weakest (log K_1 = 0.18, 2.32, 3.50, and 3.75 for $In(NO_3)_3$, $InCl_3$, InF_3, and $In(C_2H_3O_2)_3$, respectively).[36,139] A lack of direct metal-ligand bonds

in $In(NO_3)_3$ solutions is said to facilitate hydrolysis, requiring a lower energy input for metal oxide formation. There is a loose correlation between log K_1 and metal oxide (M-O) character (determined by XPS). Films from $In(NO_3)_3$ and $InCl_3$ contain > 20% more metal-oxygen bonds than those from InF_3 and $In(C_2H_3O_2)_3$ (Figure 7b). TFT device performance of resulting In_2O_3 films from $In(NO_3)_3$ exceeds that of films from the other precursors. Saturated channel mobilities (μ_{sat}) and on-off current ratios are up to two-orders-of-magnitude higher than the next-best devices from the InF_3 precursor ($In(NO_3)_3$: μ_{sat}= 24 cm^2 V^{-1} s^{-1}, $I_{on/off} = 10^8$; InF_3: μ_{sat}= 1.2 cm^2 V^{-1} s^{-1}, $I_{on/off} = 10^6$) (Figure 8b). The low μ_{sat} from $InCl_3$-based films is hypothesized to be to a result of Cl impurities due to incomplete decomposition at this 250 °C annealing temperature, despite high M-O content.

The presence of M-NO_3 complexes in thin-film precursor solutions has been correlated with degraded metal-oxide properties, despite the fact such complexes are thermodynamically weak compared to other M-*X* complexes. One reported strategy for mitigating M-NO_3 complex formation involves changing the precursor solution temperature. Lee and co-workers observe a decrease in the ratio of "free" to complexed nitrates in the Raman spectra of mixed $In(NO_3)_3/Zn(NO_3)_2$ solutions as the solution temperature is increased from 4 to 60 °C (Figure 7c).[140] The authors hypothesize that the high dielectric constant of water at lower temperatures ($\varepsilon_{H_2O} \approx$ 85 at 4 °C, compared to ~70 at 60 °C) supports greater separation of charge, thereby favoring "free" nitrate over metal nitrate complexes. However, given the majority solvent in this study is 2-methoxyethanol, which has a lower ε than water that is weakly temperature dependent ($\varepsilon \approx$ 19 at 4 °C and ~14 at 60 °C), the effect ε of should be minimal.[141] The underlying assumption is that "free" nitrate will more readily decompose from the films, resulting in a greater degree of metal-oxide condensation. Chemical analysis by XPS of the O 1s spectra show the film from the 4 °C solution has 20% greater metal-oxygen character than the film from the 60 °C solution (Figure 8c). These chemical differences are apparently responsible for higher TFT mobilities (μ) for films from the 4 °C solution (Figure 8c). A similar study, in which aqueous $In(NO_3)_3$ precursor solutions are used, also shows chemical differences (by XPS) between films prepared from chilled and room-temperature $In(NO_3)_3$ solutions.[141] However, the differences in TFT performance between films from the two different solutions are not appreciable (μ_{sat} = 0.94 cm^2 V^{-1} s^{-1} for the film from a chilled solution and 0.66 cm^2 V^{-1} s^{-1} for room temperature). High-temperature solution aging (70 °C for 72 h) has also been stated to result in increased concentration of "free" nitrates and improved metal-oxide condensation, leading to high-μ In_2O_3 TFTs (~24 cm^2 $V^{-1}s^{-1}$).[142]

The effect of precursor-solution temperature on thin-film formation chemistry is clearly complex. Mitigating M-NO_3 complexation and increasing "free" nitrate concentration appears to facilitate more-complete metal oxide condensation in the final thin film. However, the seemingly contradictory reports of improved device performance observed for films prepared from solutions that have undergone both low and high temperature treatments suggests that the dielectric of the medium may not be responsible for this effect. It is clear temperature influences M-NO_3 equilibria, which exhibits a correlation with thin-film composition and device performance. Further study is needed to elucidate how temperature-dependent equilibria influence thin-film formation processes.

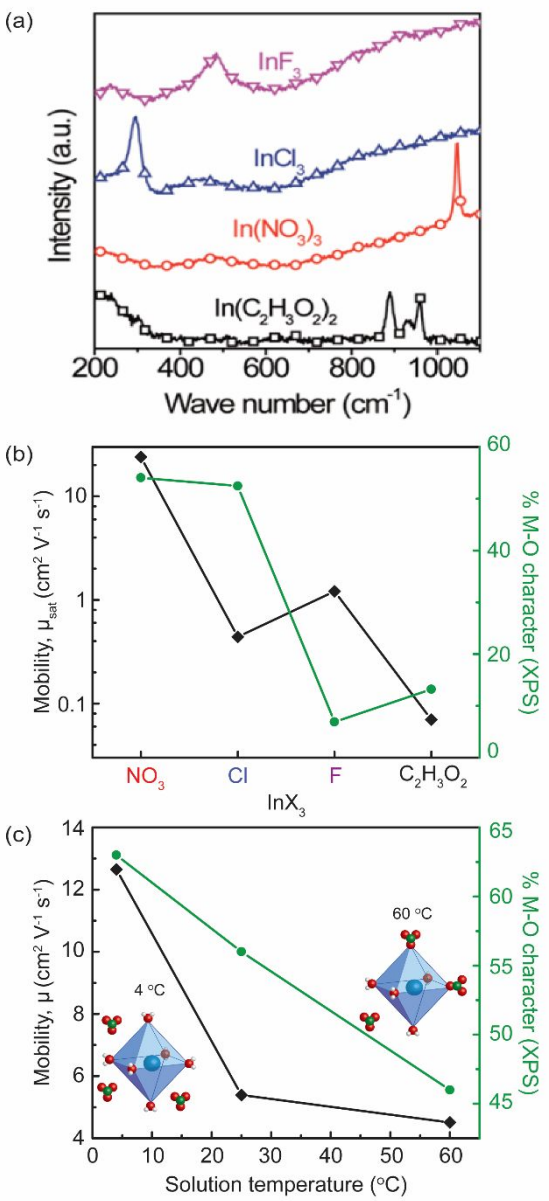

Figure 8. Metal–nitrato (M-NO_3) complex formation in thin-film solution precursors. (a) Raman spectra of aqueous indium salt (InX_3) precursor solutions. The observed vibrational modes are assigned to M-X complexes, with the exception of the peak at 1050 cm^{-1} in $In(NO_3)_3$ spectra, which is assigned to "free" nitrate. Reproduced with permission from Ref. 36. Copyright 2015 American Chemical Society. (b) TFT μ_{sat} and M-O content in In_2O_3 films from various indium precursors (data adapted from Ref. 36). The high μ_{sat} for the In_2O_3 film from $In(NO_3)_3$ is a result of high metal-oxide content due to lack of M-NO_3 complex in the precursor solution, as well as few counterion impurities in the final metal oxide. (c) Relationship between precursor solution temperature, TFT channel mobility (μ) and M-O content in indium zinc oxide thin films (data adapted from Ref. [140]). As precursor solution temperature is decreased, M-O content and μ increase, which is suggested to be a result of fewer M-NO_3 complexes present as the solution is cooled. The TFT data shown are for devices that use SiO_2 as the dielectric layer.

3. The chemical evolution of metal nitrate gels: the initial stages of metal oxide thin-film formation

3.1 From solution to thin films: fundamental considerations for the preparation of metal oxide coatings

The above discussion highlights important considerations for solution-precursor preparation. The following section will elaborate on the use of these solution precursors and the reaction pathways from solution to solid-state thin films. Common thin-film solution deposition methods include spin-, spray-, and dip-coating, with many variations on each process. The physics governing material deposition from each of these methods is detailed elsewhere.[31,46,143,144] In order to deposit a uniform thin film, the substrate must first be wetted with solution (Figure 9, step I). In order to achieve uniform wetting, the surface must be free of organic contaminants. For aqueous solutions, the surfaces must also be sufficiently hydrophilic to achieve proper wetting and reduce the interfacial energy between the solution and substrate.[144] Eliminating organic contaminants and generating polar hydrophilic surfaces can be achieved through a variety of dry and wet chemical processes. Common surface treatments include O_2 plasma, piranha (H_2O_2/H_2SO_4), and RCA-1 (H_2O_2/NH_4OH) cleaning methods. When choosing a surface treatment method, possible damage to the substrate through chemical degradation and/or physical roughening should be considered, which can negatively affect film and device properties. Once a favorable interaction between the solution and substrate is achieved, gel formation is initiated by solvent evaporation to begin the drying process (Figure 9, step II). This is accomplished via rapid substrate rotation in spin-coating and heating of the substrate during spray-coating, for example. At the end of the coating process, a concentrated metal-nitrate gel film is adhered to the substrate. In order to convert the gel into a metal-oxide thin film, remaining solvent must be evaporated (continuation of step II), nitrates removed/decomposed via HNO_3 and NO_x gas formation (Figure 9, step III), and metal-hydroxide groups condensed to form the metal oxide (M-O-M) network (Figure 9, step IV). These remaining steps require energy input, often in the form of thermal annealing.

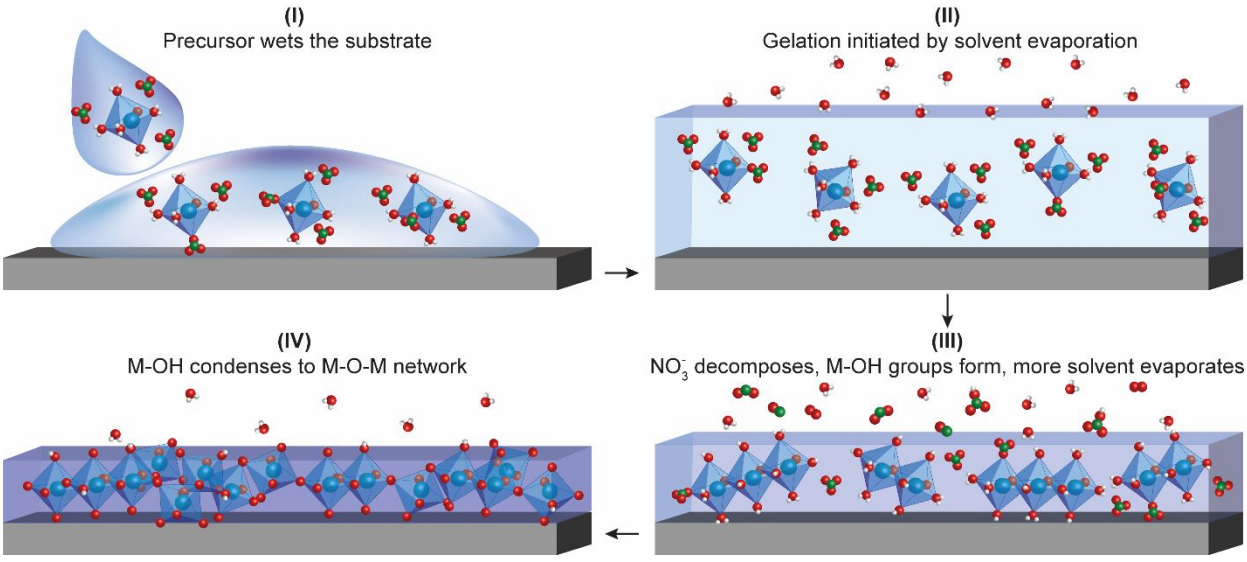

Figure 9. Stages of thin-film formation from solution precursors. (I) The substrate is wetted with an aqueous metal nitrate solution. Adequate wetting is achieve via substrate surface preparation treatments to remove organic contaminants and introduce polar functional groups to impart hydrophilicity. (II) The thin-film precursor gel is formed by rapid evaporation of excess solvent (H_2O, in this example). The resulting metal-nitrate gel must then be decomposed to form a metal oxide. (III) With addition of energy (commonly thermal annealing), additional solvent is evaporated and nitrates decompose to HNO_3, NO_x, etc. Condensation is initiated, forming $M(OH)_x$ species. (IV) Once

nitrates and solvent are removed, $M(OH)_x$ further condense to form the final metal oxide. See Figure 1a for representative chemical reactions for nitrate decomposition and hydroxyl condensation.

Controlling the reaction rates (and mechanisms) taking place in steps II-IV is crucial for controlling film morphology and structure (density, porosity, grain size, etc.), which ultimately influence device performance. If condensation of the rigid metal oxide network occurs rapidly, evaporation and decomposition byproducts will disrupt the network.[31,56] For example, as discussed previously, films from $Sn(II)(OH)_x(NO_3)_y$ nanocluster precursors exhibit rapid decomposition, resulting in nanoporosity.[47] Film morphology is also sensitive to annealing ramp rate. We observe for lanthanum zirconium oxide (LZO) films from nitrate salts that, as the temperature ramp rate is decreased from 125 to 0.25 °C min^{-1}, the films contain fewer voids and are denser. As the ramp rate slows, nitrate decomposition and hydroxide condensation are temporally separated.[54] This is a general consideration in the preparation of thin films from solution precursors. The film-formation steps II-IV often overlap substantially. While difficult to control, the temporal overlap can be decreased in many cases by controlling the thermal processing parameters (i.e. ramp/hold profiles), which provide opportunities for optimizing final film properties.

In order to exercise greater control over film formation, which will influence the resulting film structure and properties, it is important to understand the decomposition behavior of nitrates in thin-film gels. In the following section, we discuss insights gained from studying thin-film reaction pathways as a function of temperature, as thermal energy is central to most processing methods currently used.

3.2 Characterization of the metal oxide thin-film reaction pathway

Metal nitrates are generally thermally unstable and decompose at modest annealing temperatures (Figure 2). As annealing temperature increases, solvent, nitrates, and impurities are increasingly removed and metal-oxide content increases. Film evolution as a function of temperature can be evaluated using a variety of characterization techniques. Here we highlight chemical insights gained from the thermal decomposition behavior of metal-nitrate gel films to elucidate the thin-film reaction pathway.

When studying thin-film reaction pathways, it is important to know at what temperatures decomposition processes occur. While TGA of bulk precursors can provide a good estimate of the oxide formation temperature, thin films have been shown to decompose at lower annealing temperatures than their bulk counterparts.[145] Higher surface-area-to-volume ratios of nanoscale thin films compared to bulk powders leads to efficient mass and thermal transport through the thin film, which results in faster decomposition kinetics.[145,146] Therefore, studying thin-film thermal analysis directly is important for understanding decomposition behavior. Traditional TGA has been successfully adapted to studies on films 300-500 nm thick; however, greater sensitivity is required to probe small mass changes in films below 100 nm thick, which are relevant thicknesses for many electronic applications. Quartz-crystal microbalance (QCM) analysis, which has $ng \cdot cm^{-2}$ sensitivity and has been used extensively applied to studies of vapor-phase film deposition[147] as well as dissolution of electrode films during electrochemistry,[148] is a good candidate for studying small mass changes during annealing of solution-processed thin films. The effect of temperature on the crystal resonator must be accounted for in the application of QCM mass monitoring. The temperature range accessible is limited by a phase transition at 573 °C, above which the crystal loses its piezoelectric properties;[147] practically, we find this temperature limit is ~ 300 °C, where thermal shock can result in cracking. Additionally, quartz resonators have a temperature-dependent frequency response. Therefore, to decouple effects from temperature and mass loss, we have

performed these experiments ex situ (i.e. "step-wise" annealing the QCM with a deposited film at a fixed temperature, then returning to room temperature to measure the frequency following each annealing step). In principle, such limitations could be addressed to perform in situ thermal analysis on thin films using a resonator material with a small temperature coefficient, such as gallium orthophosphate ($GaPO_4$), and reliable temperature response calibration.[147] We have successfully applied ex situ QCM thermal analysis thin-film mass loss below 300 °C.[32,47,72] An example of QCM mass loss data can be seen for films from $Sn(II)(OH)_x(NO_3)_y$ nanocluster precursors in Figure 10a.[47] Mass loss for films is complete by 225 °C, whereas a 400 °C annealing temperature is needed to convert commonly-used bulk precursors to SnO_2.[149]

Because film properties are sensitive to chemical composition, studying thin-film chemical evolution is important for preparing thin films with desired properties. While thermal analysis by QCM is useful to understand when decomposition reactions occur, current-resolution limits resulting from of ex situ measurements (i.e. step-wise annealing) makes assessing decomposition mechanisms difficult. Chemical characterization techniques are needed to obtain a more complete picture of film formation reactions. The vibrational modes of nitrate, water, hydroxide, and metal-oxide bonds make FT-IR spectroscopy a convenient tool for monitoring the chemical composition as a function of annealing temperature. Representative FT-IR data that demonstrates the chemical evolution of a mixed $La(NO_3)_3/ZrO(NO_3)_2$ precursor for the preparation of lanthanum zirconium oxide (LZO) is shown in Figure 9b. Nitrate can be identified by a split N-O stretching mode, with bands centered at ~ 1300-1400 and 1600-1700 cm^{-1}. The splitting originates from a reduction of symmetry (D_{3h} to C_{2v}) due to covalent character between nitrate and the metal and/or different binding modes (monodentate, bidentate, or bridging).[150] Weaker vibrational modes, associated with M-NO_3 complexes, are at ~ 1000 and 800 cm^{-1}.[151] Water is identified by the OH stretch (~3500 cm^{-1}) and the H-O-H bending mode[152] (~1650 cm^{-1}); intensities of these modes decrease dramatically at low annealing temperatures (~ 200-300 °C). Once most of the nitrate and free water are gone, the OH stretch can be attributed primarily to metal hydroxides and the appearance of a weak, broad, metal-oxide stretch is observed near 700-800 cm^{-1}.

In addition to studying the evolution of thin-film chemical composition, decomposition byproducts can provide useful mechanistic insight into film formation. Temperature-programmed desorption mass spectrometry (TPD-MS), a tool that has been used extensively in materials science to study interactions between absorbed gases and solid surfaces, has recently been applied to thin-film formation studies from solution precursors.[153–157] While TPD studies of metal-nitrate-based films are limited,[54,72,158] there is a wealth of literature on decomposition mechanisms of adsorbed nitrate on metal-oxide surfaces. While metal oxides with surface-adsorbed nitrates and metal nitrate thin-film gels are not analogous materials, there are similarities (described below) between the nitrate decomposition pathways observed by TPD-MS for both systems.

Two distinct nitrate decomposition events have been identified in the TPD literature from studies of nitrates on metal-oxide surfaces. The first (mechanism I) is a lower-temperature event that can be identified by the evolution of NO^+ (m/z = 30) as the primary fragment, with minor contributions from N_2^+ (28), N_2O^+ (44), and NO_2^+ (46).[159] The products that evolve by mechanism I are hypothesized to originate from "loosely-bound" nitrate. Corroborative FT-IR studies suggest bidentate (chelating and/or bridging) metal-nitrate complexes contribute to this decomposition mechanism.[159,160] At higher temperatures (mechanism II), NO^+ and O_2^+ (m/z = 32) evolution are concomitant, and are associated with decomposition of nitrates that are more thermally stable, such as monodentate or ionic nitrates.[159–161]

For films prepared from metal-nitrate precursors, we similarly identify two distinct nitrate decomposition and desorption events by TPD-MS. A detailed discussion of metal-nitrate decomposition chemistry can be found in Section *2.1 Bulk metal nitrate chemistry*, along with representative chemical in Figure 1a. Because we are unable to definitively assign IR-active nitrate modes from thin films to specific binding motifs (Figure 10b), we do not assign these fragments as originating from specific nitrate environments. In addition to the fragments described by mechanism I, we observe H_2O^+ (m/z =18) accompanying this first nitrate decomposition event, which may suggest the H_2O/HNO_3 azeotrope contributes to the film decomposition pathway (Figure 1a, eqn i).[72] For mechanism II, we believe these fragments are associated with the thermal decomposition of "tightly-bound" nitrate (Figure 1a, eqn ii), likely M-NO_3 complexes. TPD-MS fragments produced from a $Y(NO_3)_3$ precursor are representative of fragmentation patterns typically observed from nitrate decomposition byproducts that evolve from thin-film samples (Figure 10c).

Once nitrate is effectively eliminated from the film, XPS is useful to continue studying film evolution. The degree of metal oxide condensation can be evaluated as a function of annealing temperature through analysis of the O 1s regional spectrum. Three oxygen environments are commonly fit for metal-oxide thin-films: metal oxide (528-531 eV, denoted O_I), "oxygen vacancies" (531-532 eV, O_{II}), and metal hydroxide (531-534 eV, O_{III}) (Figure 11a).[34,36,162–165] Sometimes referred to as "oxygen-deficient states," the O_{II} region encompasses under-coordinated metal atoms due to sub-stoichiometric compositions, as well as weakly-bound impurities from adsorbed gases, residual nitrate, adventitious carbon, etc.[162–164] For nitrate precursors, the metal-oxygen peak area increases with annealing temperature and there exists a linear correlation between the metal-oxygen peak area and In_2O_3 TFT mobility (Figure 11b).[34,36,165] Increased μ is facilitated by improved condensation at increased annealing temperature, as well as "clean" nitrate decomposition (i.e. few impurities remaining in the film), which facilitates densification.[36]

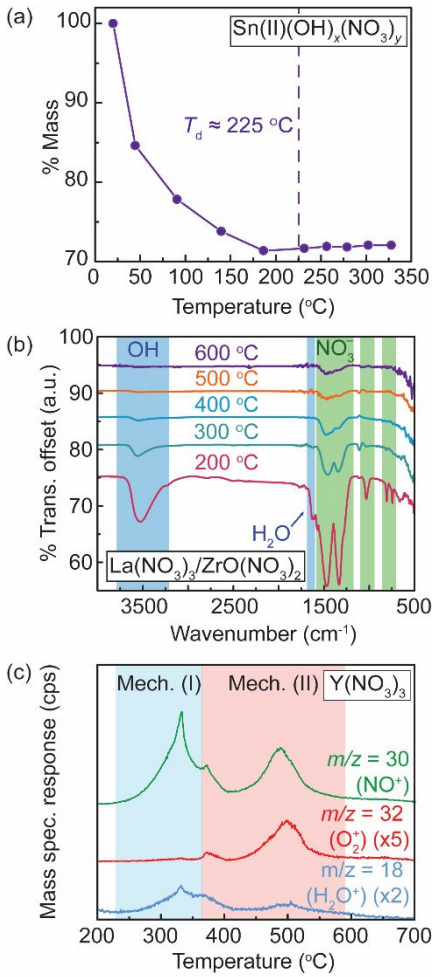

Figure 10. Characterization techniques to study the metal-oxide thin-film reaction pathway by thermal annealing. (a) Quartz-crystal-microbalance (QCM) thermal-analysis data is used to determine thin-film decomposition temperatures (T_d). The above example shows the T_d of a thin film from the $Sn(II)(OH)_x(NO_3)_y$ nanocluster precursor was estimated to be ~ 225 °C (data from Ref. 47). (b) Chemical composition of thin films as a function of annealing temperature can be monitored by Fourier transform infrared (FT-IR) spectroscopy, due to the intense nitrate IR active modes. Representative data of an FT-IR annealing study is shown for films from a $La(NO_3)_3/ZrO(NO_3)_2$ (1 La : 1 Zr) precursor for lanthanum zirconium oxide (LZO) films. These data are adapted from Ref. 36. (c) Thin-film decomposition products can be studied using temperature-programmed-desorption mass spectrometry (TPD-MS). Two distinct nitrate-decomposition mechanisms can be inferred from the data shown for $Y(NO_3)_3$ thin films. Mechanism I (highlighted in blue) is associated with "loosely-bound" nitrate, including HNO_3/H_2O azeotrope, as evidenced by concomitant detection of NO^+ and H_2O^+ fragments. Mechanism II (highlighted in red) is associated with nitrate in more thermally stable environments and are identified by simultaneous detection of NO^+ and O_2^+ fragments. These data are adapted from Ref. 72.

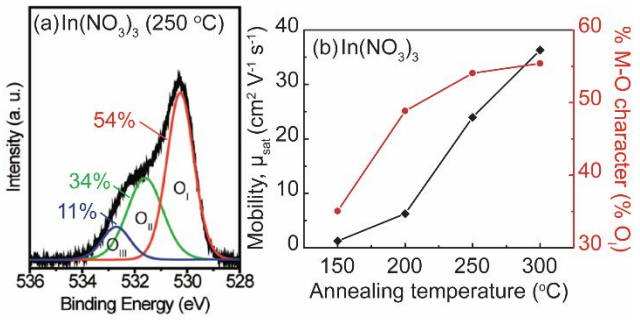

Figure 11. Evaluating quality of metal oxides from metal-nitrate precursors. (a) O 1s XPS spectrum from an In_2O_3 film indicating oxygen environments typically observed in metal-oxide thin films. The O_I, O_{II}, and O_{III} environments, as denoted in the figure, are assigned to indium oxide (In-O), oxygen vacancies (i.e. nitrate (N-O), carbon (C-O), under-coordinated oxygen species, etc.), and indium hydroxide (In-OH), respectively. (b) Metal-oxide character and In_2O_3 TFT saturated channel mobility (μ_{sat}) increase with annealing temperature for films from $In(NO_3)_3$. Higher μ_{sat} at higher annealing temperatures is a result of increased M-O content and fewer nitrate impurities remaining in the film. The TFT data shown are for devices that use SiO_2 as the dielectric layer. Data reproduced and adapted with permission from Ref. 36. Copyright 2015 American Chemical Society.

3.3 Alternatives to conventional thermal processing: a survey of low-temperature processing methods utilizing unique metal nitrate chemistries

Because of their relatively low decomposition temperatures, metal nitrate precursors have been extensively used in the development of low-temperature solution-processing methods. Various chemical strategies have been introduced to produce high-quality metal-oxide thin films with a reduced thermal budget. The primary objective of so-called "low-temperature processing" methods is to improve compatibility of solution processing with low-melting point, inexpensive polymeric substrates. Here, we highlight progress made toward low-temperature processing by utilizing the unique reactivity of nitrate with alternative energy sources and annealing atmospheres.

3.3.1 Combustion processing

The combustion processing method, first introduced by Kim et. al,[52] endeavors to use the internally-produced exothermic heat from a combustion reaction between nitrate and an organic fuel. This approach is intended to lower thin-film processing temperatures relative to metal nitrate thermal decomposition reaction, which is an endothermic process. Figure 12a depicts a reaction coordinate diagram demonstrating the difference between combustion and thermal decomposition. Since the combustion process is highly exothermic, this change to the reaction enthalpy (ΔH) leads to a comparatively more spontaneous ΔG. Mild annealing conditions (~ 200-300 °C) are purported to ignite a combustion front that propagates through the thin-film volume. High local temperatures produced by this reaction (reported to be upward of 1000 °C for bulk systems, depending on the oxidizer-fuel mixture used[166]) are hypothesized to decompose nitrate and condense the oxide network. Combustion processing is, in principle, compatible with low-melting-point polymeric substrates because the high surface-area-to-volume ratio of the film rapidly dissipates heat to the atmosphere.[52] Since the first report of thin-film combustion processing, which focused primarily on $In(NO_3)_3$-based precursors using acetylacetone and urea fuels,[52] the method has been applied to many other metal nitrate and fuel systems.[50,51,167–176]

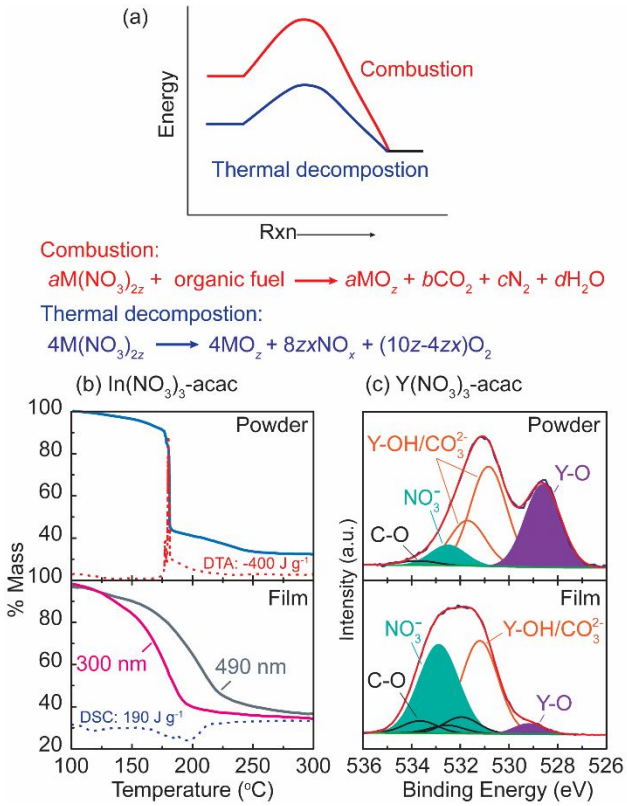

Figure 12. Reactivity of combustion precursors. (a) Reaction coordinate diagram depicting combustion and thermal decomposition pathways with their associated chemical reactions. Combustion is considered a low-temperature thin-film processing method because low applied temperatures (compared to thermal decomposition) lead to ignition of an exothermic combustion front. It is suggested the heat produced by combustion decomposes nitrates and condenses the metal-oxide network. (b) TGA comparison for a bulk powder (top) and thin film (bottom) prepared from the combustible mixture $In(NO_3)_3$ -acac. An exotherm (i.e. combustion) is detected for the bulk powder, whereas an endotherm (i.e. thermal decomposition) is detected for the thin film. Data adapted from Ref. [146]. (c) O 1s XP spectra for a powder and film prepared from a $Y(NO_3)_3$-acac mixture by annealing at the combustion ignition temperature. Composition analysis suggests combustion occurs in the powder (i.e. high Y-O, low NO_3^- content) but not in the thin film (i.e. low Y-O, high NO_3^-) when samples are annealed above the combustion ignition temperature (215 °C). Data adapted from Ref. 72.

The combustion method has been applied to a variety of films for TFTs[170–176] and photovoltaic applications.[50,51,169] In order to benchmark the performance of combustion-processed films relative to other common solution-deposition approaches, we compare here TFT derived electron mobilities μ of In_2O_3 films (Figure 13). Combustion-synthesized films demonstrate respectable μ improvements compared to sol-gel films (i.e. 2-methoxyethanol solvent without combustion additives), especially when spray-deposited.[176] However, In_2O_3 films from aqueous precursors exhibit up to an order of magnitude higher μ than combustion and sol-gel films annealed at comparable temperatures. This is likely a result of increased densification and fewer carbon impurities in the films made from aqueous $In(NO_3)_3$ precursors.[33]

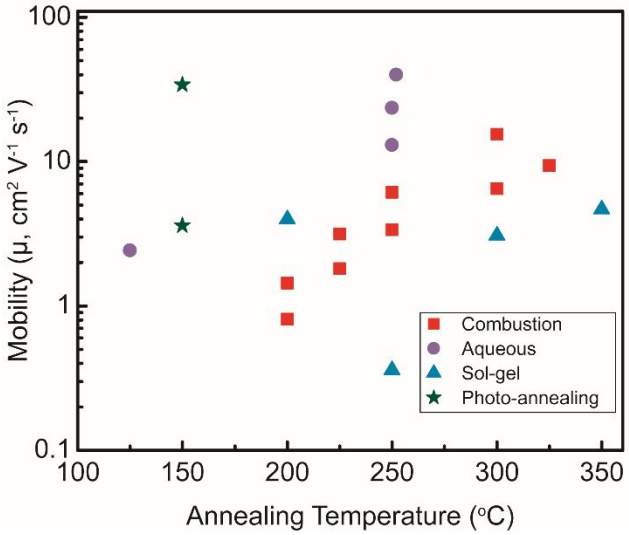

Figure 13. Comparison of In_2O_3 films prepared by various low-temperature processing methods. Channel mobilities (μ) for In_2O_3 TFTs are used to compare properties prepared using various low-temperature processing strategies. All data presented here are for TFTs with SiO_2 dielectric layers, for ease of comparison. The associated references for the data categories plotted above are as follows: combustion,[52,176] aqueous,[36,142,177,178] sol-gel,[179,180] and photo-annealing.[53,181]

For selective-contact applications in solar cells, combustion-processed thin films have demonstrated improved performance over other commonly-used methods/precursors. When paired with an organic absorber, combustion-synthesized NiO films perform similarly to widely-used organic hole-transport layers (HTLs), with power conversion efficiencies (PCE) of 1.6 and 1.7%, respectively, and outperforms NiO from a nickel acetate precursor (0.16%).[169] In another study, PCEs for combustion (17.7%) and sol-gel (15.5%) Cu-doped NiO films exhibit similar performance at drastically-reduced processing temperatures (150 and 500 °C, respectively).[51] Additionally, combustion-derived IGO and IGZO films have been shown to have electronic structures that are tunable with composition, which demonstrates a design strategy for engineering charge-carrier selective contacts that can be tailored to match valence and conduction band energies of various absorber materials.[50] It should be noted, however, that direct comparisons in the literature of thin films from combustion precursors (metal nitrates with fuels) and metal nitrates without fuels are lacking; therefore, it is impossible to attribute the improved solar cell performance to combustion processing directly.

The number of examples of metal oxides prepared by the combustion method shows these precursors are useful for making solution-processed films/devices of reasonable quality. However, several studies have called into question the fundamental chemistry of combustion reactions in thin films.[72,146,182–184] The $In(NO_3)_3$-acetylacetone (or "acac") mixture, first studied by Kim,[52] was investigated by TGA in both the bulk and thin-film form.[146] Combustion is identified by an abrupt mass loss event, accompanied by an exotherm in the differential thermal analysis (DTA) signal, which is evident for the bulk system (Figure 12b, top). In contrast, gradual mass loss and an endotherm, associated with thermal decomposition, are detected for a thin film prepared from the same precursor, suggesting combustion does not occur (Figure 12b, bottom). To investigate this observed difference in bulk and thin-film reactivity, we studied the chemical composition and thermal behavior of several model combustion-precursor systems. When we applied the thin-film QCM technique to $In(NO_3)_3$- and $Y(NO_3)_3$-acac precursors, we similarly observed gradual mass loss with annealing temperature, which is an indicator of thermal decomposition rather than

combustion.[72] Additionally, XPS analysis of powders and films prepared from $Y(NO_3)_3$-acac show significant chemical differences when annealed at the combustion ignition temperature (T_{ig} ~ 200 °C). While the powder contains high Y-O content, the thin film contains comparatively low Y-O and retains significant $Y(NO_3)_3$ precursor character (Figure 12c). Incorporation of fuel into the precursor solutions does not improve precursor conversion to the corresponding metal oxide for thin films at lower processing temperatures, as it does in the bulk, suggesting combustion does not occur in thin films.

Computational modeling to simulate the decomposition kinetics and heat conduction in thin films corroborates experimental data that suggests thin-film combustion does not occur.[146,182–184] When modeled in the geometry of a bulk powder in a crucible, combustible mixtures exhibit an inhomogeneous reaction rate throughout the sample volume, consistent with combustion front propagation.[146] When the same precursor is modeled in the geometry of a thin film, a combustion front is not observed. Numerical modeling of reaction kinetics suggests that, in order to overcome the activation energy for combustion in a 1-μm-thick film, the substrate temperature and ramp rate must be at least 1200 K and 10^7 K min^{-1}, respectively.[184] These values are determined using expressions that exhibit strong dependence on the height-to-radius ratio of the sample (the sample volume is approximated as that of a cylinder) and the critical mass, which is dependent on the thermal conductivity of the sample/substrate. Therefore, even when the same combustion precursors are used in the preparation of bulk and thin-film metal oxides, differences in thermal transport result in different reaction pathways.

In light of the experimental and computational results discussed here, thin-film combustion of metal nitrates at low temperatures is unlikely. Rather, the various improvements in device performance obtained when the combustion thin-film synthesis is used may be attributed to other factors, namely, the high volatility of metal nitrate decomposition products. Most studies compare films prepared from combustion precursors to those from metal chlorides and/or acetates,[51,52,169] which decompose at higher temperatures and leave non-volatile impurities in the metal oxide thin films.[34,36] Additionally, some studies have observed fuels can improve film morphology, which can also positively influence device performance. NiO films from a $Ni(NO_3)_2$-urea precursor are smoother than those from $Ni(C_2H_3O_2)_4$ (AFM R_{rms} roughness of 1.1 and 12.3 nm, respectively).[169] In our previous studies on combustion, films from the $In(NO_3)_3$-acac precursor show enhanced crystallinity by x-ray diffraction (XRD) compared to films from $In(NO_3)_3$, indicating fuel incorporation can influence the nanoscale structure of films.[72] Indeed, there may be ways in which film properties benefit from the use of "combustion" precursors, even without combustion reactions occuring.

3.3.2 Ultraviolet (UV) photo-annealing

A unique aspect of metal-nitrate chemistry is the susceptibility of nitrates to decomposition when irradiated with deep-ultraviolet (UV) light (λ = 185-254 nm). This chemistry has been applied to thin-film formation and is known as "photo-annealing" (Figure 14a).[53] The mechanism of nitrate removal from thin films was confirmed to be nitrate photolysis (eq. 10), through UV-visible and NMR studies on UV-irradiated $Al(NO_3)_3$ solutions.[185] The oxygen radical produced in eq. 10 further reacts with water to form hydroxyl species (eqn. 11), which can condense to form metal oxides.

$$NO_3^- \xrightarrow{h\nu} {}^\bullet NO_2 + O^{\bullet -} \qquad (10)$$

$$O^{\bullet -} + H_2O \leftrightharpoons {}^\bullet OH + OH^- \qquad (11)$$

This reaction scheme is consistent with previous literature on UV-wastewater treatment to decompose nitrate.[186,187] In thin films, the radicals produced by nitrate photolysis are hypothesized to decompose organic solvents and form M-OH groups. While photo-annealing effectively eliminates nitrates from thin films at room temperature, moderate annealing treatments (~150-200 °C), facilitated by radiant heat from UV lamp operation or post-UV exposure, aid condensation to the final metal-oxide phase.[53,188] FT-IR spectroscopy confirms nitrates are removed from $Al(NO_3)_3$, as evidenced by disappearance of N-O vibrational modes (1340 and 1440 cm^{-1}) after 5 min of UV exposure (Figure 14b). In contrast, films from $Al(NO_3)_3$ thermally annealed at 150 °C for up to 120 min still exhibit intense N-O stretching modes, indicating photolysis enhances nitrate decomposition over moderate thermal annealing conditions.

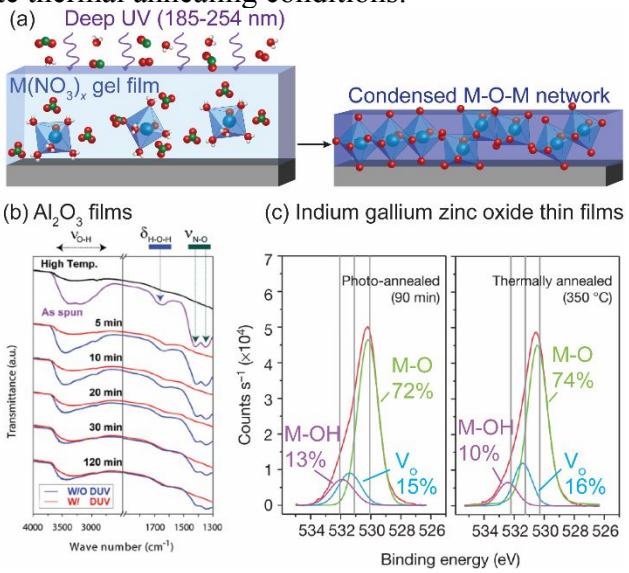

Figure 14. Photo-annealing of metal-nitrate gel films. (a) Schematic of the photo-annealing reaction. UV light decomposes nitrates to various volatile NO_x products via photolysis. Photon energy from the UV source, as well as heat from operation of the UV lamp (~ 150 °C), facilitate condensation of $M(OH)_x$ to metal oxide. (b) FT-IR spectra of $Al(NO_3)_3$ films photo- and thermally-annealed (at 150 °C) as a function of irradiation/annealing time. IR active modes for nitrate are no longer visible after 5 min of photo-annealing (red), whereas nitrates are still present in thermally-annealed films (blue) after a 2 h annealing time. Reproduced with permission from Ref. 185. Copyright 2015 John Wiley & Sons. (c) Fitted O 1s XP spectra comparing the oxygen chemical environments present in photo- and thermally-annealed (350 °C) indium-gallium-zinc-oxide (IGZO) films. Photo-annealed films are chemically similar to films thermally-annealed at high temperature, which suggests photo-annealing is an effective low-temperature processing method for preparing IGZO with high metal oxide content. Reprinted with permission from Ref. 53. Copyright 2012 Nature Publishing Group.

Kim et al. demonstrated the photo-annealing effect on IGZO films prepared from the nitrate salts.[53] In this study, photo-annealed films were shown to have comparable metal-oxide content (determined by XPS) to films thermally annealed at 350 °C (Figure 14c). Similar optical band gaps ($E_g \approx 3.2$ eV) and higher average channel mobilities ($\mu \sim 9$ cm^2 V^{-1} s^{-1} compared to ~ 6 cm^2 V^{-1} s^{-1}) further confirm relatively high-performance metal oxides can be prepared via this method. Mobilities of >30 cm^2 V^{-1} s^{-1} for photo-annealed In_2O_3 and IZO channel layers have since been reported.[181] Such improvements to device performance are attributed to O_3 production during photolysis, which is suggested to mediate oxygen-vacancy formation in the resulting thin films, thereby reducing trap states.[189,190] The channel mobilities for photo-annealed films are comparable to (or even greater than) than those achieved for aqueous, sol-gel, and combustion In_2O_3 films

annealed at temperatures of 200 °C or higher, indicating photo-annealing is an effective low-temperature processing method for high-quality electronic thin films (Figure 13).

Since these initial studies, photo-annealing has demonstrated applicability to the preparation of many semiconductor and dielectric thin films for electronics,[37,45,185,191] as well as catalyst films for the oxygen-evolution reaction.[192] Aside from low metal-oxide formation temperatures, photo-annealing treatments have been correlated with increased densification.[191,193] Denser films result in higher areal capacitance for dielectrics and higher carrier mobilities for semiconductors in TFTs. Additionally, photo-annealed films are observed to have low interfacial roughness due to improved wetting of subsequent layers, leading to a reduction of interfacial trap states.[185] Interestingly, films from flat-"Al_{13}" nanocluster precursors photo-annealed at 60 °C exhibit a high breakdown fields (> 6 MV cm^{-1}) and respectable dielectric constants (κ = 8.37) in contrast to similarly-treated films from $Al(NO_3)_3$ precursor, which produce non-functional MIM devices at this annealing temperature.[194] Jo et al. suggest the pre-condensed M-O-M network of "Al_{13}" and lower counterion content of the solution enable greater densification of the Al_2O_3 film, which leads to improved insulating properties (2.58 and 1.86 g cm^{-3} for "Al_{13}" cluster and $Al(NO_3)_3$ prepared films, respectively).

While there are numerous studies that utilize the photo-annealing method to prepare high-quality thin films, it is worth noting that nearly all systems studied to date are "low-T_d" metal nitrate salts. As discussed in *2.1 Bulk metal nitrate chemistry*, thermal decomposition behavior has a strong dependence on the metal cation. An interesting area of future work would involve studying the UV-susceptibility of "high-T_d" salts to determine if photolysis behavior exhibits a metal dependence similar to that observed for thermal decomposition.

3.3.3 Controlled-atmosphere annealing: the role of water vapor in film formation

In addition to using different energy sources for metal oxide formation, reactions of film components with atmospheric gases have also shown promise for lowering processing temperatures. Approaches include annealing under O_3, high pressure, and vacuum, which were discussed in depth in a recent review;[195] however, these annealing atmospheres are primarily used once the metal oxide has already formed, rather than to influence film formation chemistry. Here, we focus on the relatively underexplored water-vapor annealing process, which has been demonstrated to facilitate film formation from a variety of solution precursors. For metal-alkoxide precursors, water facilitates removal of organic residues and improves metal-oxide conversion, resulting in high channel mobilities for In-based TFTs (~ 30 cm^2 V^{-1} s^{-1}).[196,197] A similar effect was reported for ZnO films from a $Zn(NH_3)_4^{2+}$ precursor.[198] A steady supply of water vapor is hypothesized to enhance the rate of hydrolysis of coordinating ligands by ensuring water is not a limiting reagent. Interestingly, one study investigates the effect of humidity on film formation from sol-gel (i.e. 2-methoxyethanol) metal-nitrate precursors; however, the authors do not comment on the reactions of nitrates with atmospheric water.[197]

We reported the effects of water-saturated "humid" atmosphere annealing on films from all-inorganic aqueous precursors, which we refer to as the "steam-annealing" process.[54] Advantages of steam annealing, compared to ambient "dry" annealing, are threefold: (1) enhanced nitrate removal at low annealing temperatures (< 200 °C), (2) improved resistance to water reabsorption, and (3) increased densification. The most striking reduction of nitrate content is observed in lanthanum zirconium oxide (LZO) films annealed at temperatures as low as 200 °C.[54] We hypothesized that nitrate removal was facilitated by maintaining the hydration sphere of the metal ions, thereby inhibiting the formation of M-NO_3 complexes, which require higher temperatures to decompose. An excess of water also favors the removal of nitrate through the HNO_3/H_2O

azeotrope (with a boiling point of 120 °C), offering an alternative pathway to thermal decomposition for "loosely-bound" nitrates. This hypothesis is supported by TPD-MS data, which shows a distinct difference in the annealing temperatures at which NO^+ decomposition fragments are observed, especially at temperatures below 400 °C (Figure 15a). Steam-annealed films are also resistant to post-processing water reabsorption, another indication of enhanced nitrate removal, as nitrates are hygroscopic. FT-IR spectra of steam- and dry-annealed films, collected immediately following annealing and again after 1 h in ambient, show significant water absorption for the dry-annealed film compared to the steam-annealed one (Figure 15b). A comparison of the N-O stretching region intensities in the FT-IR spectra shows that steam-annealed films contain fewer nitrates.

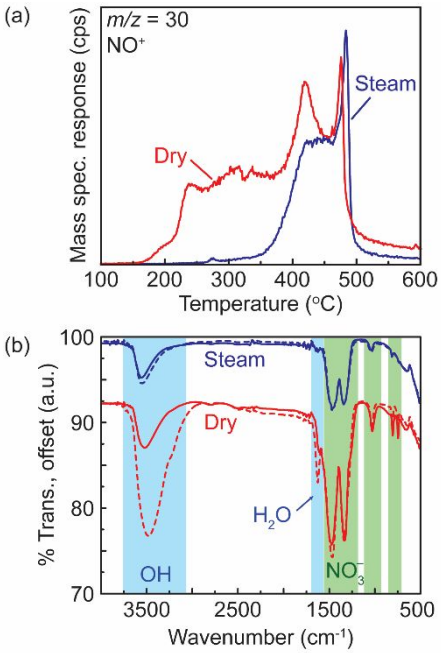

Figure 15. Chemical analysis of steam- and dry-annealed films. (a) A comparison of the NO^+ fragment (m/z = 30) desorption profile observed for dry- and steam-annealed LZO films (200 °C). A reduction in signal below 400 °C for steam- compared to dry-annealed films is associated with enhanced nitrate removal. (b) FT-IR spectra of films annealed at 200 °C (solid lines), then left in ambient for 1 h (dotted lines). While dry-annealed films absorb water, as evidenced by the increased intensity of the OH stretching mode, steam-annealed films are moisture resistant. Data adapted from Ref. 54.

Enhanced nitrate removal via steam annealing also increases film density. Cross-sectional scanning-electron-microscope (SEM) images confirm steam-annealed films are 15% thinner than dry-annealed films (Figure 16). Differences in film chemistry at or near the surface may influence densification processes. We hypothesize, for steam-annealed films, that water helps maintain surface hydroxyl groups, which allow for facile diffusion of HNO_3 and other decomposition byproducts out of the film (Figure 16a). In contrast, enhanced dehydration at the dry film surface may result in a dense surface layer that inhibits mass transport, resulting in thicker, lower-density films (Figure 16b).[199,200]

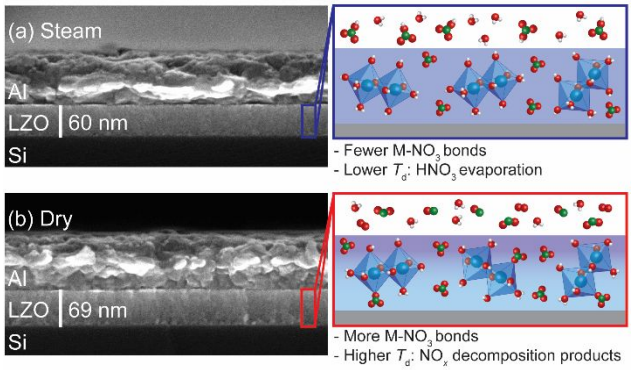

Figure 16. Improved densification of steam-annealed films. SEM images of (a) steam- and (b) dry-annealed films. The schematics show the different decomposition products that are hypothesized to form under each atmosphere (i.e. HNO_3 from steam-annealing and NO_x gases from dry-annealing), as well as the formation of a "surface crust" in dry-annealed films, which we hypothesize inhibits densification.

The benefits of steam annealing on film composition and morphology led to higher dielectric constants (κ) for LZO films in metal-insulator-semiconductor (MIS) devices. The κ for MIS devices prepared from 500 °C dry-annealed films is comparable to that of 350 °C steam-annealed films (κ = 15 at 1 kHz). Notably, MIS devices prepared from 200 °C dry-annealed films are nonfunctional dielectrics, while steam-annealed films fabricated at the same temperature exhibit modest dielectric constants (κ = 11 at 1 kHz). In contrast to our reports of improved device performance for humid-annealed dielectrics, a previous study reported a degradation in the dielectric response of Al_2O_3 with increased relative humidity (RH) of the annealing environment ($Al(NO_3)_3$ precursor).[201] Devices prepared from films annealed at 0% RH environment experience lower leakage currents and higher breakdown voltages than those annealed at 60% RH. A similar effect was observed for In_2O_3 channel mobility. The authors suggest high humidity inhibits condensation by favoring metal hydroxyl species in the metal hydroxide/oxide equilibria. However, the films characterized in this study were of noticeably poor morphology. Optical microscope images show increasing defects on the film surface as RH is increased, likely due to water droplets disturbing the film surface. High surface roughness is known to negatively impact TFT performance, and a roughness as small as a few nanometers has been shown to decrease field-effect mobility up to an order of magnitude.[202–204] For this reason it is critical to completely aerosolize and evaporate water for steam-annealing studies, as is done in our work, in order to avoid degrading film morphology under a humid atmosphere.

4. Outlook: toward implementation of solution-processed metal-oxide films in manufacturing

In this review, we have discussed ways in which the unique aspects of metal-nitrate chemistry have been used to facilitate the development of high-quality, solution-processed metal-oxide thin films. Detailed knowledge of the chemical interactions and reactions that influence metal-oxide film formation is important for the future integration of solution deposition into industrial manufacturing. David Mitzi, in his book, *Solution Processing of Inorganic Materials*,[27] discusses six primary drivers needed to enable solution-processed inorganic materials in an industrial setting. Here we discuss how each of the following drivers can be addressed by utilizing and controlling metal-nitrate chemistry:

4.1 Low cost per unit area and large area-deposition (Drivers 1 & 2)

In many ways, metal-nitrate precursors are ideal candidates for large-scale production of solution-processed coatings. Metal-nitrate salts are generally inexpensive; however, scalable synthetic methods for metal-nitrate-based precursors have the potential to further decrease raw materials cost. We demonstrated a dissolution approach for the preparation of flat-"Al_{13}" nanocluster precursors from HNO_3 digestion of the abundant, inexpensive $Al(OH)_3$ gibbsite mineral (~ \$0.04 mol^{-1}, compared to ~ \$0.3 mol^{-1} for $Al(NO_3)_3 \bullet 9H_2O$ at 2019 bulk international commodity prices) and demonstrated its usefulness as a Al_2O_3 film precursor.[118] One could imagine extension of this approach to other mineral, hydroxide, or oxide systems to reduce cost and generate large quantities of metal-nitrate precursors.

Another aspect of metal-nitrate chemistry with potential to further address cost is their UV susceptibility (see *3.3.2 Ultraviolet (UV) photo-annealing*), which makes these precursors "self-patterning."[205,206] Because photo-annealing is an oxide-forming reaction, exposure through a shadow mask results in selected-area metal-oxide condensation to pattern the functional material. Therefore, there is potential to utilize such reactions to eliminate photolithography steps.

Solution processing is compatible with a variety of high-volume, ambient processing deposition techniques. The ability to deposit metal oxides via spray-coating, ink-jet, slot-die, etc. makes solution deposition an attractive option for low-cost, large-area deposition technologies, such as roll-to-roll processing.

4.2 Ability to deposit on diverse substrates (Driver 3)

The development of low-temperature processing methods, including those discussed in this review, have potential to improve compatibility of solution-deposited thin films with temperature-sensitive substrates. In particular, low-T_d nitrate salts (i.e. In, Ga, Zn, and Al nitrates) have already demonstrated some level of compatibility with low-melting point polymeric substrates.[52,53,193,207] There are comparatively few examples of effective low-temperature processing methods for their high-T_d counterparts (i.e. Y and La).[208,209] Therefore, there remains substantial opportunity to design processes to lower decomposition temperatures for such materials, including further investigations of UV photo-annealing and steam annealing. A particularly under-explored area of thin-film processing chemistry is that of alternative annealing atmospheres. As discussed in *2.1 Bulk metal-nitrate chemistry*, metal-nitrate decomposition exhibits a strong dependence on the surrounding ambient. Introduction of different gases to control decomposition kinetics and reaction pathways could provide additional control over thin-film decomposition temperatures and resulting film properties, as we have demonstrated for steam annealing. Control over metal-nitrate decomposition chemistry is crucial for expanding the application base of solution-processed metal oxides to flexible devices.

4.3 "Adequate" electronic performance (Driver 4)

Recently, great strides have been made to improve the electronic performance of solution-deposited films, with some semiconductors and dielectrics approaching quality equivalent to vacuum-deposited films.[32,41,176,178] The electronic properties of the films are sensitive to impurities (i.e. residual counterions and hydroxides), density, morphology and degree of crystallinity and crystallite size. Improvements to electronic properties rely heavily on designing processes that leverage control over metal-nitrate chemistry, both in solution and during film formation. As is clear from the wide range of chemical processes that influence the thin-film reaction pathway,

controlling these processes this is not simple. Complete impurity removal is imperative for maximizing metal-oxide condensation and density. The most-effective strategies demonstrated in the literature thus far include the use of nanocluster precursors and steam annealing, which both result in fewer counterions in the resulting film and enhanced film densification. Control over film morphology/crystallinity would additionally improve electronic performance. In cases where amorphous materials are preferred (for example in the dielectric layers of TFTs), crystallization can often be suppressed by controlling multi-metal composition and annealing conditions.

4.4 High yield, low variability (Driver 5)

Devices from solution-processed thin films are often afflicted by low yield and high variability. While these are primarily process-engineering challenges to be addressed during production ramp, consideration of precursor chemistry has been utilized to address such issues on a laboratory scale. Many of the studies highlighted in this review demonstrate how the chemical nature of precursors influences thin-film electronic performance (i.e. hydrolysis products, solution temperature, purity, etc.). An understanding of how concentration, temperature, and pH influence solution chemistry could decrease lot-to-lot variation and inform how precursor conditions affect film properties. Additionally, as was demonstrated for electrochemically-treated IGZO precursors, purposeful and controlled changes to solution chemistry can improve film homogeneity by preventing phase segregation, which is a source of variability.[32] While some "M_{13}"-type nanoclusters are thermodynamic products,[116] there are likely many metal-hydroxo nanoclusters throughout the periodic table that are kinetic products,[47,136] which may present additional scale-up and storage challenges that would need to be addressed in order to maintain batch-to-batch consistency.

4.5 Long-term stability and durability (Driver 6).

Long-term stability of metal-oxide films produced from metal-nitrate precursor solutions is strongly dependent on successful elimination of hygroscopic nitrate counterions. Additionally, some metal oxides are prone to water absorption (i.e. La_2O_3),[210] which can be exacerbated by residual nitrate in thin films. This is another area in which chemistry can be used to improve processing conditions to impart improved thin-film stability. We have shown steam-annealing metal-nitrate-based thin films improves moisture resistance. We attribute the enhanced ambient stability of steam-annealed films to differences in the chemical and physical properties compared to dry-annealed films, namely fewer residual nitrates and improved densification.[54] Another strategy to improve thin-film stability toward water involves incorporating moisture-resistant components into the film using capping layers or preparing ternary metal-oxide compositions. Thin capping layers of HfO_2[211,212] and ZrO_2[213] on hygroscopic metal-oxide thin films have also proven to be successful strategies for inhibiting water uptake. Our research groups have developed aqueous routes for the preparation of lanthanum zirconium and lanthanum aluminum oxides (LZO, $LaAlO_3$) from metal-nitrate precursors, which exhibit reduced hygroscopicity compared to La_2O_3.[39,40] Apart from water absorption, ternary metal-oxide compositions can improve stability toward other impurities. LZO thin films are more resistant to atmospheric carbonate absorption compared to La_2O_3,[40,54] whereas $LaAlO_3$ contains fewer hydrogen impurities than Al_2O_3,[214] which results in improved dielectric properties.

Metal-oxide thin-film stability and durability are influenced by precursor choice, processing conditions, and intrinsic metal-oxide properties, all of which must be considered when developing solution-deposition methods.

5. Conclusion

In this review, we have highlighted ways in which understanding metal-nitrate chemistry has contributed to the advancement of solution deposition as a method for preparing high-quality metal-oxide thin films. An examination of bulk metal-nitrate chemistry demonstrates decomposition behavior is sensitive to the metal identity and the annealing atmosphere, which has implications for selecting processing conditions that optimize metal oxide formation in thin films. Solution-speciation chemistry exhibits a complex dependence on concentration, pH, and temperature and can influence film properties, including density, homogeneity, and chemical composition. Some unique aspects of metal-nitrate reactivity, such as UV and humid-atmosphere susceptibility, are utilized to enhance nitrate removal and metal-oxide conversion during thin-film formation. Continued improvement of our understanding of metal-nitrate chemistry will further aid process optimization to facilitate high-volume manufacturing of high-quality metal oxide thin films for (opto)electronic applications.

Conflicts of interest

The authors declare no conflicts of interest.

Author Information

Corresponding authors
*email: dwj@uoregon.edu
*email: cpage@uoregon.edu
*email: swb@uoregon.edu

ORCID
Darren W. Johnson: 0000-0001-5967-5115
Catherine J. Page: 0000-0002-4545-7835
Shannon W. Boettcher: 0000-0001-8971-9123

Acknowledgements

This work was supported by the NSF Center for Sustainable Materials Chemistry (CHE-1606982). This work was also supported by the Bradshaw and Holzapfel Research Professorship in Transformational Science and Mathematics to D.W.J. E.A.C. thanks Forrest A.L. Laskowski for assistance with figure preparation.

References

1 J. S. Park, W. J. Maeng, H. S. Kim and J. S. Park, *Thin Solid Films*, 2012, **520**, 1679–1693.
2 A. Liu, H. Zhu, H. Sun, Y. Xu and Y. Noh, *Adv. Mater.*, 2018, **30**, 1706364.
3 E. Fortunato, P. Barquinha and R. Martins, *Adv. Mater.*, 2012, **24**, 2945–2986.
4 S. C. Dixon, D. O. Scanlon, C. J. Carmalt and I. P. Parkin, *J. Mater. Chem. C*, 2016, **4**, 6946–6961.
5 A. N. Banerjee and K. K. Chattopadhyay, *Prog. Cryst. Growth Charact. Mater.*, 2005, **50**,

52–105.
6 M. Lorenz, M. S. Ramachandra Rao, T. Venkatesan, E. Fortunato, P. Barquinha, R. Branquinho, D. Salgueiro, R. Martins, E. Carlos, A. Liu, F. K. Shan, M. Grundmann, H. Boschker, J. Mukherjee, M. Priyadarshini, N. DasGupta, D. J. Rogers, F. H. Teherani, E. V Sandana, P. Bove, K. Rietwyk, A. Zaban, A. Veziridis, A. Weidenkaff, M. Muralidhar, M. Murakami, S. Abel, J. Fompeyrine, J. Zuniga-Perez, R. Ramesh, N. A. Spaldin, S. Ostanin, V. Borisov, I. Mertig, V. Lazenka, G. Srinivasan, W. Prellier, M. Uchida, M. Kawasaki, R. Pentcheva, P. Gegenwart, F. Miletto Granozio, J. Fontcuberta and N. Pryds, *J. Phys. D. Appl. Phys.*, 2016, **49**, 433001.
7 X. Yu, T. J. Marks and A. Facchetti, *Nat. Mater.*, 2016, **15**, 383–396.
8 X. Yang, Q. Bi, H. Ali, K. Davis, W. V. Schoenfeld and K. Weber, *Adv. Mater.*, 2016, **28**, 5891–5897.
9 X. Yin, C. Battaglia, Y. Lin, K. Chen, M. Hettick, M. Zheng, C. Y. Chen, D. Kiriya and A. Javey, *ACS Photonics*, 2014, **1**, 1245–1250.
10 E. J. Juarez-Perez, M. Wußler, F. Fabregat-Santiago, K. Lakus-Wollny, E. Mankel, T. Mayer, W. Jaegermann and I. Mora-Sero, *J. Phys. Chem. Lett.*, 2014, **5**, 680–685.
11 P. P. Boix, J. Ajuria, I. Etxebarria, R. Pacios, G. Garcia-Belmonte and J. Bisquert, *J. Phys. Chem. Lett.*, 2011, **2**, 407–411.
12 M. S. White, D. C. Olson, S. E. Shaheen, N. Kopidakis and D. S. Ginley, *Appl. Phys. Lett.*, 2006, **89**, 143517.
13 C. Battaglia, X. Yin, M. Zheng, I. D. Sharp, T. Chen, S. McDonnell, A. Azcatl, C. Carraro, B. Ma, R. Maboudian, R. M. Wallace and A. Javey, *Nano Lett.*, 2014, **14**, 967–971.
14 A. K. K. Kyaw, X. W. Sun, C. Y. Jiang, G. Q. Lo, D. W. Zhao and D. L. Kwong, *Appl. Phys. Lett.*, 2008, **93**, 2006–2009.
15 K. X. Steirer, J. P. Chesin, N. E. Widjonarko, J. J. Berry, A. Miedaner, D. S. Ginley and D. C. Olson, *Org. Electron.*, 2010, **11**, 1414–1418.
16 X. Xu, Z. Liu, Z. Zuo, M. Zhang, Z. Zhao, Y. Shen, H. Zhou, Q. Chen, Y. Yang and M. Wang, *Nano Lett.*, 2015, **15**, 2402–2408.
17 Y. Wang, E. L. Runnerstrom and D. J. Milliron, *Annu. Rev. Chem. Biomol. Eng.*, 2016, **7**, 283–304.
18 C. G. Granqvist, *Thin Solid Films*, 2014, **564**, 1–38.
19 Z. Fan, C. C. Chao, F. Hossein-Babaei and F. B. Prinz, *J. Mater. Chem.*, 2011, **21**, 10903–10906.
20 X. Chen, N. J. Wu, L. Smith and A. Ignatiev, *Appl. Phys. Lett.*, 2004, **84**, 2700–2702.
21 A. S. Asundi, J. A. Raiford and S. F. Bent, *ACS Energy Lett.*, 2019, **4**, 908–925.
22 M. G. Kast, L. J. Enman, N. J. Gurnon, A. Nadarajah and S. W. Boettcher, *ACS Appl. Mater. Interfaces*, 2014, **6**, 22830–22837.
23 R. D. L. Smith, M. S. Prevot, R. D. Fagan, Z. Zhang, P. A. Sedach, M. K. J. Siu, S. Trudel and C. P. Berlinguette, *Science*, 2013, **340**, 60–63.
24 L. Trotochaud, J. K. Ranney, K. N. Williams and S. W. Boettcher, *J. Am. Chem. Soc.*, 2012, **134**, 17253–17261.
25 T. P. St. Clair and D. W. Goodman, *Top. Catal.*, 2000, **13**, 5–19.
26 H. J. Freund and G. Pacchioni, *Chem. Soc. Rev.*, 2008, **37**, 2224–2242.
27 D. B. Mitzi, Ed., *Solution Processing of Inorganic Materials*, John Wiley & Sons Inc., Hoboken, 1st edn., 2009.
28 K. M. Kim, C. W. Kim, J. S. Heo, H. Na, J. E. Lee, C. B. Park, J. U. Bae, C. D. Kim, M.

Jun, Y. K. Hwang, S. T. Meyers, A. Grenville and D. A. Keszler, *Appl. Phys. Lett.*, 2011, **99**, 242109.
29 W. Xu, H. Li, J. Bin Xu and L. Wang, *ACS Appl. Mater. Interfaces*, 2018, **10**, 25878–25901.
30 C. J. Brinker and G. W. Scherer, *Sol-Gel Science: The Physics and Chemistry of Sol-Gel Processing*, Academic Press, Inc., Boston, 1st edn., 1990.
31 R. W. Schwartz, T. Schneller and R. Waser, *Comptes Rendus Chim.*, 2004, **7**, 433–461.
32 A. Nadarajah, M. Z. B. Wu, K. Archila, M. G. Kast, A. M. Smith, T. H. Chiang, D. A. Keszler, J. F. Wager and S. W. Boettcher, *Chem. Mater.*, 2015, **27**, 5587–5596.
33 K.-H. Lim, J. Lee, J.-E. Huh, J. Park, J.-H. Lee, S.-E. Lee and Y. S. Kim, *J. Mater. Chem. C*, 2017, **5**, 7768–7776.
34 S. Jeong, J. Y. Lee, S. S. Lee, Y. Choi and B. H. Ryu, *J. Phys. Chem. C*, 2011, **115**, 11773–11780.
35 W. J. Scheideler, R. Kumar, A. R. Zeumault and V. Subramanian, *Adv. Funct. Mater.*, 2017, **27**, Article No. 1606062.
36 Y. S. Rim, H. Chen, T.-B. Song, S.-H. Bae and Y. Yang, *Chem. Mater.*, 2015, **27**, 5808–5812.
37 G. Liu, A. Liu, H. Zhu, B. Shin, E. Fortunato, R. Martins, Y. Wang and F. Shan, *Adv. Funct. Mater.*, 2015, **25**, 2564–2572.
38 A. Liu, G. X. Liu, H. H. Zhu, F. Xu, E. Fortunato, R. Martins and F. K. Shan, *ACS Appl. Mater. Interfaces*, 2014, **6**, 17364–17369.
39 P. N. Plassmeyer, K. Archila, J. F. Wager and C. J. Page, *ACS Appl. Mater. Interfaces*, 2015, **7**, 1678–1684.
40 K. N. Woods, T. H. Chiang, P. N. Plassmeyer, M. G. Kast, A. C. Lygo, A. K. Grealish, S. W. Boettcher and C. J. Page, *ACS Appl. Mater. Interfaces*, 2017, **9**, 10897–10903.
41 C. K. Perkins, M. Jenkins, T.-H. Chiang, R. H. Mansergh, V. Goulioukk, N. Kenane, J. Wager, J. F. Conley and D. A. Keszler, *ACS Appl. Mater. Interfaces*, 2018, **10**, 36082–36087.
42 K. N. Woods, E. C. Waddington, C. A. Crump, E. A. Bryan, T. S. Gleckler, M. R. Nellist, B. A. Duell, D. P. Nguyen, S. W. Boettcher and C. J. Page, *RSC Adv.*, 2017, **7**, 39147–39152.
43 A. Liu, G. Liu, H. Zhu, H. Song, B. Shin, E. Fortunato, R. Martins and F. Shan, *Adv. Funct. Mater.*, 2015, **25**, 7180–7188.
44 A. Liu, G. Liu, H. Zhu, B. Shin, E. Fortunato, R. Martins and F. Shan, *RSC Adv.*, 2015, **5**, 86606–86613.
45 C. Zhu, A. Liu, G. Liu, G. Jiang, Y. Meng, E. Fortunato, R. Martins and F. Shan, *J. Mater. Chem. C*, 2016, **4**, 10715–10721.
46 R. M. Pasquarelli, D. S. Ginley and R. O. Hayre, *Chem. Soc. Rev.*, 2011, **40**, 5406–5441.
47 A. Nadarajah, M. E. Carnes, M. G. Kast, D. W. Johnson and S. W. Boettcher, *Chem. Mater.*, 2013, **25**, 4080–4087.
48 P. Richter, P. N. Plassmeyer, J. Harzdorf, T. Rüffer, H. Lang, J. Kalbacova, N. Jöhrmann, S. Schulze, M. Hietschold, S. S. P. K. Arekapudi, M. Albrecht, D. R. T. Zahn, C. J. Page and G. Salvan, *Chem. Mater.*, 2016, **28**, 4917–4927.
49 D. R. Clayton, D. Lepage, P. N. Plassmeyer, C. J. Page and M. C. Lonergan, *RSC Adv.*, 2017, **7**, 7046–7051.
50 N. Zhou, M.-G. Kim, S. Loser, J. Smith, H. Yoshida, X. Guo, C. Song, H. Jin, Z. Chen, S. M. Yoon, A. J. Freeman, R. P. H. Chang, A. Facchetti and T. J. Marks, *Proc. Natl. Acad.*

Sci., 2015, **112**, 7897–7902.
51 J. W. Jung, C. C. Chueh and A. K. Y. Jen, *Adv. Mater.*, 2015, **27**, 7874–7880.
52 M.-G. Kim, M. G. Kanatzidis, A. Facchetti and T. J. Marks, *Nat. Mater.*, 2011, **10**, 382–388.
53 Y.-H. Kim, J.-S. Heo, T.-H. Kim, S. Park, M.-H. Yoon, J. Kim, M. S. Oh, G.-R. Yi, Y.-Y. Noh and S. K. Park, *Nature*, 2012, **489**, 128–132.
54 K. N. Woods, P. N. Plassmeyer, D. H. Park, L. J. Enman, A. K. Grealish, B. L. Kirk, S. W. Boettcher, D. A. Keszler and C. J. Page, *Chem. Mater.*, 2017, **29**, 8531–8538.
55 Y. S. Rim, S. H. Bae, H. Chen, N. De Marco and Y. Yang, *Adv. Mater.*, 2016, **28**, 4415–4440.
56 I. Bretos, R. Jiménez, J. Ricote and M. L. Calzada, *Chem. Soc. Rev.*, 2018, **47**, 291–308.
57 S. Yuvaraj, F. Y. Lin, T. H. Chang and C. T. Yeh, *J. Phys. Chem. B*, 2003, **107**, 1044–1047.
58 M. Wolters, H. Daly, A. Goguet, F. C. Meunier, C. Hardacre, J. H. Bitter, P. E. De Jongh and K. P. De Jong, *J. Phys. Chem. C*, 2010, **114**, 7839–7845.
59 Y. Li and B. W. L. Jang, *Ind. Eng. Chem. Res.*, 2010, **49**, 8433–8438.
60 M. R. Quddus, M. M. Hossain and H. I. De Lasa, *Catal. Today*, 2013, **210**, 124–134.
61 P. Melnikov, V. A. Nascimento, I. V. Arkhangelsky, L. Z. Zanoni Consolo and L. C. S. De Oliveira, *J. Therm. Anal. Calorim.*, 2013, **111**, 543–548.
62 P. Melnikov, V. A. Nascimento and L. Z. Z. Consolo, *J Therm Anal Calorim*, 2012, **107**, 1117–1121.
63 P. Melnikov, V. A. Nascimento, L. Z. Z. Consolo and A. F. Silva, *J. Therm. Anal. Calorim.*, 2013, **111**, 115–119.
64 P. Melnikov, V. A. Nascimento, I. V Arkhangelsky, L. C. S. de Oliveira, A. F. Silva and L. Z. Z. Consolo, *J Therm Anal Calorim*, 2014, **119**, 1073–1079.
65 A. J. Kozak, *J. Therm. Anal. Calorim.*, 1999, **58**, 647–651.
66 W. W. Wendlandt and J. L. Bear, *J. Inorg. Nucl. Chem.*, 1960, **12**, 276–280.
67 P. K. Gallagher and D. W. Johnson Jr., *J. Electrochem. Soc.*, 1971, **118**, 1530–1534.
68 A. Małecki and B. Małecka, *Thermochim. Acta*, 2006, **446**, 113–116.
69 J. Zhuang, Q. J. Sun, Y. Zhou, S. T. Han, L. Zhou, Y. Yan, H. Peng, S. Venkatesh, W. Wu, R. K. Y. Li and V. A. L. Roy, *ACS Appl. Mater. Interfaces*, 2016, **8**, 31128–31135.
70 B. Yang, G. He, L. Zhu, C. Zhang, Y. Zhang, Y. Xia, F. Alam and Z. Sun, *ACS Appl. Electron. Mater.*, 2019, **1**, 625–636.
71 M. G. Kast, E. A. Cochran, L. J. Enman, G. Mitchson, J. Ditto, C. Siefe, P. N. Plassmeyer, A. L. Greenaway, D. C. Johnson, C. J. Page and S. W. Boettcher, *J. Am. Chem. Soc.*, 2016, **138**, 16800–16808.
72 E. A. Cochran, D.-H. Park, M. G. Kast, L. J. Enman, C. K. Perkins, R. H. Mansergh, D. A. Keszler, D. W. Johnson and S. W. Boettcher, *Chem. Mater.*, 2017, **29**, 9480–9488.
73 R. D. Shannon, *Acta Crystallogr. Sect. A*, 1976, **32**, 751–767.
74 J. Schefer and M. Grube, *Mater. Res. Bull.*, 1995, **30**, 1235–1241.
75 D. Lazar, B. Ribár and B. Prelesnik, *Acta Crystallogr. Sect. C Cryst. Struct. Commun.*, 1991, **47**, 2282–2285.
76 A. D. Hendsbee, C. C. Pye and J. D. Masuda, *Acta Crystallogr. Sect. E Struct. Reports*, 2009, **65**, i65.
77 M. A. Malyarik, S. P. Petrosyants, A. B. Ilyukhin and Y. A. Buslaev, *Zhurnal Neorg. Khimii*, 1993, **38**, 1975–1980.
78 T. J. Boyle, J. M. Sears, M. L. Neville, T. M. Alam and V. G. Young, *Inorg. Chem.*, 2015,

54, 11831–11841.
79 D. Lazar, B. Ribár, V. Divjaković and C. Mészáros, *Acta Crystallogr. Sect. C Cryst. Struct. Commun.*, 1991, **47**, 1060–1062.
80 D. Popov, R. Herak, N. Radulovic and B. Ribar, *Zeitschrift für Krist.*, 1975, **142**, 347–355.
81 N. J. Hair and J. K. Beattie, *Inorg. Chem.*, 1977, **16**, 245–250.
82 P. V. Prelesnik, F. Gabela, B. Ribar and I. Krstanovic, *Acta Crystallogr. Sect. C Cryst. Struct. Commun.*, 1973, **2**, 581–583.
83 F. Bigoli, A. Braibanti, A. Tiripicchio and M. T. Camellini, *Acta Crystallogr. Sect. B Struct. Crystallogr. Cryst. Chem.*, 1971, **27**, 1427–1434.
84 B. Morosin, *Acta Crystallogr. Sect. B Struct. Crystallogr. Cryst. Chem.*, 1970, **26**, 1203–1208.
85 V. B. Ribar and W. Nowacki, *Zeitschrift für Krist.*, 1970, **131**, 175–185.
86 B. Ribar, N. Milinski, Z. Budovalcev and I. Krstanovic, *Acta Crystallogr. Sect. C Cryst. Struct. Commun.*, 1980, **9**, 203–206.
87 P. Bénard, M. Louër and D. Louër, *J. Solid State Chem.*, 1991, **94**, 27–35.
88 A. Gobichon, M. Loue, D. Loue and J. P. Auffre, *J. Solid State Chem.*, 1996, **126**, 127–134.
89 N. Milinski, P. Radivojevic, B. Ribar and S. Djuric, *Acta Crystallogr. Sect. C Cryst. Struct. Commun.*, 1982, **11**, 1241–1244.
90 D. J. Rogers, N. J. Taylor and G. E. Toogood, *Acta Crystallogr. Sect. C Cryst. Struct. Commun.*, 1983, **39**, 939–941.
91 R. Kawashima, M. Sasaki, S. Satoh, H. Isoda, Y. Kino and Y. Shiozak, *J. Phys. Soc. Japan*, 2000, **69**, 3297–3303.
92 S. Stockhause and G. Meyer, *Zeitschrift für Krist.*, 1997, **212**, 315.
93 G. Shengli, M. Huairang and Y. Zupei, *Xibei Daxue Xuebao, Ziran Kexueban*, 1990, **20**, 53–58.
94 C. Rincke, H. Schmidt and W. Voigt, *Zeitschrift fur Anorg. und Allg. Chemie*, 2017, **643**, 437–442.
95 A.-E. Gobichon, J.-P. Auffrékdic and D. Louër, *Solid State Ionics*, 1997, **93**, 51–64.
96 W. Wang, I.-Y. Chang, L. Zakharov, P. H.-Y. Cheong and D. A. Keszler, *Inorg. Chem.*, 2013, **52**, 1807–1811.
97 J. R. A. Sietsma, J. D. Meeldijk, J. P. Den Breejen, M. Versluijs-Helder, A. J. Van Dillen, P. E. De Jongh and K. P. De Jong, *Angew. Chemie - Int. Ed.*, 2007, **46**, 4547–4549.
98 B. Małecka, A. Łącz, E. Drozdz and A. Małecki, *J. Therm. Anal. Calorim.*, 2015, **119**, 1053–1061.
99 K. N. Woods, D. M. Hamann and C. J. Page, *Solid State Sci.*, 2018, **75**, 34–38.
100 J. Livage, *Catal. Today*, 1998, **41**, 3–19.
101 W. W. Rudolph, D. Fischer, M. R. Tomney and C. C. Pye, *Phys. Chem. Chem. Phys.*, 2004, **6**, 5145–5155.
102 W. W. Rudolph and G. Irmer, *Dalt. Trans.*, 2015, **44**, 18492–18505.
103 W. W. Rudolph and G. Irmer, *Dalt. Trans.*, 2015, **44**, 295–305.
104 G. Wulfsberg, *Inorganic Chemistry*, University Science Books, Sausalito, 1st edn., 2000.
105 M. Henry, J. P. Jolivet and J. Livage, in *Chemistry, Spectroscopy and Applications of Sol-Gel Glasses. Structure and Bonding, vol. 77*, eds. R. Reisfeld and C. K. JJørgensen, Springer, Berlin, 1992, pp. 153–206.
106 R. E. Mesmer and C. F. Baes, *MRS Proc.*, 1990, **281**, 935–962.
107 D. T. Richens, *The Aqueous Chemistry of Aqua Ions*, John Wiley & Sons, Ltd, Chichester,

England, 1st edn., 1997.
108 C. F. Baes and R. E. Mesmer, *The Hydrolysis of Cations*, John Wiley & Sons Inc., New york, 1976.
109 M. Pourbaix, *Atlas of Electrochemical Equilibria in Aqueous Solutions*, Pergamon Press, Oxford, 1st edn., 1966.
110 G. K. Schweitzer and L. L. Pesterfield, *The aqueous chemistry of the elements*, Oxford University Press, Oxford, 2013, vol. 48.
111 M. N. Jackson, M. K. Kamunde-Devonish, B. A. Hammann, L. A. Wills, L. B. Fullmer, S. E. Hayes, P. H. Y. Cheong, W. H. Casey, M. Nyman and D. W. Johnson, *Dalt. Trans.*, 2015, **44**, 16982–17006.
112 M. K. Kamunde-Devonish, M. N. Jackson, Z. L. Mensinger, L. N. Zakharov and D. W. Johnson, *Inorg. Chem.*, 2014, **53**, 7101–7105.
113 C. K. Perkins, E. S. Eitrheim, B. L. Fulton, L. B. Fullmer, C. A. Colla, D. H. Park, A. F. Oliveri, J. E. Hutchison, M. Nyman, W. H. Casey, T. Z. Forbes, D. W. Johnson and D. A. Keszler, *Angew. Chemie - Int. Ed.*, 2017, **56**, 10161–10164.
114 L. Allouche, C. Gerardin, T. Loiseau, G. Ferey and F. Taulelle, *Angew. Chemie - Int. Ed.*, 2000, **39**, 511–514.
115 G. Biedermann and D. Ferri, *Acta Chem. Scand. A*, 1982, **36**, 611–622.
116 L. A. Wills, X. Qu, I. Y. Chang, T. J. L. Mustard, D. A. Keszler, K. A. Persson and P. H. Y. Cheong, *Nat. Commun.*, 2017, **8**, 1–7.
117 J. Livage, M. Henry and C. Sanchez, *Prog. Solid State Chem.*, 1988, **18**, 259–341.
118 B. L. Fulton, C. K. Perkins, R. H. Mansergh, M. A. Jenkins, V. Gouliouk, M. N. Jackson, J. C. Ramos, N. M. Rogovoy, M. T. Gutierrez-Higgins, S. W. Boettcher, J. F. Conley, D. A. Keszler, J. E. Hutchison and D. W. Johnson, *Chem. Mater.*, 2017, **29**, 7760–7765.
119 W. Wang, W. Liu, I.-Y. Chang, L. A. Wills, L. N. Zakharov, S. W. Boettcher, P. H.-Y. Cheong, C. Fang and D. A. Keszler, *Proc. Natl. Acad. Sci. U. S. A.*, 2013, **110**, 18397–401.
120 W. W. Rudolph, R. Mason and C. C. Pye, *Phys. Chem. Chem. Phys.*, 2000, **2**, 5030–5040.
121 W. W. Rudolph and C. C. Pye, *Phys. Chem. Chem. Phys.*, 2002, **4**, 4319–4327.
122 Y. Marcus, *J. Chem. Soc. Faraday Trans.*, 1991, **87**, 2295–2999.
123 F. P. Rotzinger, *J. Am. Chem. Soc.*, 1997, **119**, 5230–5238.
124 S. Kobayashi, S. Nagayama and T. Busujima, *J. Am. Chem. Soc.*, 1998, **120**, 8287–8288.
125 L. Helm and A. E. Merbach, *Dalt. Trans.*, 2002, 633–641.
126 A. E. Danks, S. R. Hall and Z. Schnepp, *Mater. Horizons*, 2016, **3**, 91–112.
127 Z. Wang, U. Helmersson and P. O. Käll, *Thin Solid Films*, 2002, **405**, 50–54.
128 Q. Fan, B. McQuillin, A. K. Ray, M. L. Turner and A. B. Seddon, *J. Phys. D. Appl. Phys.*, 2000, **33**, 2683–2686.
129 J.-B. Seo, Y. H. Cho, W. H. Lee, J.-H. Lee, Y. S. Kim and K. Char, *Japan Soc. Appl. Phys.*, 2019, **12**, Article No. 071004.
130 E. Rather, J. T. Gatlin, P. G. Nixon, T. Tsukamoto, V. Kravtsov and D. W. Johnson, *J. Am. Chem. Soc.*, 2005, **127**, 3242–3243.
131 Z. L. Mensinger, J. T. Gatlin, S. T. Meyers, L. N. Zakharov, D. A. Keszler and D. W. Johnson, *Angew. Chemie - Int. Ed.*, 2008, **47**, 9484–9486.
132 J. T. Gatlin, Z. L. Mensinger, L. N. Zakharov, D. Macinnes and D. W. Johnson, *Inorg. Chem.*, 2008, **47**, 1267–1269.
133 A. J. Bard, R. Parsons and J. Jordan, *Standard Potentials in Aqueous Solution*, International Union of Pure and Applied Chemistry, 1st edn., 1985.

134 W. Wang, K. M. Wentz, S. E. Hayes, D. W. Johnson and D. A. Keszler, *Inorg. Chem.*, 2011, **50**, 4683–4685.

135 M. N. Jackson, L. A. Wills, I. Y. Chang, M. E. Carnes, L. F. Scatena, P. H. Y. Cheong and D. W. Johnson, *Inorg. Chem.*, 2013, **52**, 6187–6192.

136 D. A. Marsh, S. Goberna-Ferrón, M. K. Baumeister, L. N. Zakharov, M. Nyman and D. W. Johnson, *Dalt. Trans.*, 2017, **46**, 947–955.

137 M. E. Carnes, C. C. Knutson, A. Nadarajah, M. N. Jackson, A. F. Oliveri, K. M. Norelli, B. M. Crockett, S. R. Bauers, H. A. Moreno-Luna, B. N. Taber, D. J. Pacheco, J. Z. Olson, K. R. Brevick, C. E. Sheehan, D. W. Johnson and S. W. Boettcher, *J. Mater. Chem. C*, 2014, **2**, 8492–8496.

138 C. K. Perkins, R. H. Mansergh, J. C. Ramos, C. E. Nanayakkara, D.-H. Park, S. Goberna-Ferrón, L. B. Fullmer, J. T. Arens, M. T. Gutierrez-Higgens, Y. R. Jones, J. I. Lopez, T. M. Rowe, D. M. Whitehurst, M. Nyman, Y. J. Chabal and D. A. Keszler, *Opt. Mater. Express*, 2017, **7**, 273–280.

139 R. M. Smith and A. E. Martell, *Critical Stability Constants*, Springer, New York, 1976, vol. 4.

140 K. H. Lee, J. H. Park, Y. B. Yoo, W. S. Jang, J. Y. Oh, S. S. Chae, K. J. Moon, J. M. Myoung and H. K. Baik, *ACS Appl. Mater. Interfaces*, 2013, **5**, 2585–92.

141 C.-M. Kang, J. H. Ryu, H. Kim, Y.-W. O. K.-H. Baek and L.-M. Do, *J. Nanosci. Nanotechnol.*, 2016, **16**, 8473–8477.

142 J. Park, T. Gergely, Y. S. Rim and S. Pyo, *ACS Appl. Electron. Mater.*, 2019, **1**, 505–512.

143 A. Liu, H. Zhu, H. Sun, Y. Xu and Y. Y. Noh, *Adv. Mater.*, 2018, **30**, 1–39.

144 P. Martin, *Handbook of Deposition Technologies for Films and Coatings: Science, Applications and Technologies*, Elsevier, Inc., Oxford, 3rd edn., 2005.

145 P. Roura, J. Farjas, S. Ricart, M. Aklalouch, R. Guzman, J. Arbiol, T. Puig, A. Calleja, O. Peña-Rodríguez, M. Garriga and X. Obradors, *Thin Solid Films*, 2012, **520**, 1949–1953.

146 D. Sanchez-Rodriguez, J. Farjas, P. Roura, S. Ricart, N. Mestres, X. Obradors and T. Puig, *J. Phys. Chem. C*, 2013, **117**, 20133–20138.

147 J. W. Elam and M. J. Pellin, *Anal. Chem.*, 2005, **77**, 3531–3535.

148 D. A. Buttry and M. D. Ward, *Chem. Rev.*, 1992, **92**, 1355–1379.

149 P. G. L. Baker, R. D. Sanderson and A. M. Crouch, *Thin Solid Films*, 2007, **515**, 6691–6697.

150 F. Vratny, *Appl. Spectrosc.*, 1959, **13**, 59–70.

151 R. A. Nyquist, C. L. Putzig, M. A. Leugers and R. O. Kagel, *The Handbook of Infrared and Raman Spectra of Inorganic Compounds and Organic Salts*, Academic Press, Inc., San Diego, CA, 1997.

152 H. A. Al-abadleh and V. H. Grassian, *Langmuir*, 2003, **19**, 341–347.

153 T. Takahashi and T. Nishide, *Jorunal Ceram. Soc. Japan*, 2004, **238**, 234–238.

154 H. Shimizu, S. Konagai, M. Ikeda and T. Nishide, *Jpn. J. Appl. Phys.*, 2009, **48**, 1011011–1011016.

155 H. Shimizu, D. Nemoto, M. Ikeda and T. Nishide, *Jpn. J. Appl. Phys.*, 2010, **49**, 1–8.

156 R. H. Mansergh, L. B. Fullmer, D. H. Park, M. Nyman and D. A. Keszler, *Chem. Mater.*, 2016, **28**, 1553–1558.

157 R. T. Frederick, J. M. Amador, S. Goberna-Ferrón, M. Nyman, D. A. Keszler and G. S. Herman, *J. Phys. Chem. C*, 2018, **122**, 16100–16112.

158 J. Cui, M. G. Kast, B. A. Hammann, Y. Afriyie, K. N. Woods, P. N. Plassmeyer, C. K.

Perkins, Z. L. Ma, D. A. Keszler, C. J. Page, S. W. Boettcher and S. E. Hayes, *Chem. Mater.*, 2018, **30**, 7456–7463.
159 Y. Chi and S. S. C. Chuang, *J. Phys. Chem. B*, 2000, **104**, 4673–4683.
160 X. Zhang, H. He, H. Gao and Y. Yu, *Spectrochim. Acta - Part A Mol. Biomol. Spectrosc.*, 2008, **71**, 1446–1451.
161 F. Prinetto, G. Ghiotti, I. Nova, L. Lietti, E. Tronconi and P. Forzatti, *J. Phys. Chem. B*, 2001, **105**, 12732–12745.
162 S. Jeong, J. Y. Lee, S. S. Lee, Y. H. Seo, S. Y. Kim, J. U. Park, B. H. Ryu, W. Yang, J. Moon and Y. Choi, *J. Mater. Chem. C*, 2013, **1**, 4236–4243.
163 X. Yu, L. Zeng, N. Zhou, P. Guo, F. Shi, D. B. Buchholz, Q. Ma, J. Yu, V. P. Dravid, R. P. H. Chang, M. Bedzyk, T. J. Marks and A. Facchetti, *Adv. Mater.*, 2015, **27**, 2390–2399.
164 Y. K. Kim, C. H. Ahn, M. G. Yun, S. W. Cho, W. J. Kang and H. K. Cho, *Sci. Rep.*, 2016, **6**, 1–9.
165 H. Wang, T. Sun, W. Xu, F. Xie, L. Ye, Y. Xiao, Y. Wang, J. Chen and J. Xu, *RSC Adv.*, 2014, **4**, 54729–54739.
166 A. Varma, A. Mukasyan, A. Rogachev and K. V Manukyan, *Chem. Rev.*, 2016, **116**, 14493–14586.
167 B. Wang, L. Zeng, W. Huang, F. S. Melkonyan, W. C. Sheets, L. Chi, M. J. Bedzyk, T. J. Marks and A. F. Facchetti, *J. Am. Chem. Soc.*, 2016, **138**, 7067–7074.
168 Y. Chen, B. Wang, W. Huang, X. Zhang, G. Wang, M. J. Leonardi, Y. Huang, Z. Lu, T. J. Marks and A. Facchetti, *Chem. Mater.*, 2018, **30**, 3323–3329.
169 Y. Zhang and Z. Li, *Ceram. Int.*, 2015, **42**, 6360–6368.
170 R. Branquinho, D. Salgueiro, L. Santos, P. Barquinha, L. Pereira, R. Martins and E. Fortunato, *ACS Appl. Mater. Interfaces*, 2014, **6**, 19592–19599.
171 Y. H. Kang, S. Jeong, J. M. Ko, J.-Y. Lee, Y. Choi, C. Lee and S. Y. Cho, *J. Mater. Chem. C*, 2014, **2**, 4247–4256.
172 Q. Jiang, L. Feng, C. Wu, R. Sun, X. Li, B. Lu, Z. Ye and J. Lu, *Appl. Phys. Lett.*, 2015, **106**, Article No. 053503.
173 J. Smith, L. Zeng, R. Khanal, K. Stallings, A. Facchetti, J. E. Medvedeva, M. J. Bedzyk and T. J. Marks, *Adv. Electron. Mater.*, 2015, **1**, Article No. 1500146.
174 J. W. Hennek, J. Smith, A. Yan, M. G. Kim, W. Zhao, V. P. Dravid, A. Facchetti and T. J. Marks, *J. Am. Chem. Soc.*, 2013, **135**, 10729–10741.
175 J. W. Hennek, M. G. Kim, M. G. Kanatzidis, A. Facchetti and T. J. Marks, *J. Am. Chem. Soc.*, 2012, **134**, 9593–9596.
176 X. Yu, J. Smith, N. Zhou, L. Zeng, P. Guo, Y. Xia, A. Alvarez, S. Aghion, H. Lin, J. Yu, R. P. H. Chang, M. J. Bedzyk, R. Ferragut, T. J. Marks and A. Facchetti, *Proc. Natl. Acad. Sci.*, 2015, **112**, 3217–3222.
177 Y. H. Hwang, J. S. Seo, J. M. Yun, H. J. Park, S. Yang, S. H. K. Park and B. S. Bae, *NPG Asia Mater.*, 2013, **5**, Article No. e45.
178 I. Isakov, H. Faber, M. Grell, G. Wyatt-Moon, N. Pliatsikas, T. Kehagias, G. P. Dimitrakopulos, P. P. Patsalas, R. Li and T. D. Anthopoulos, *Adv. Funct. Mater.*, 2017, **27**, 1–9.
179 J. S. Lee, Y.-J. Kwack and W.-S. Choi, *ACS Appl. Mater. Interfaces*, 2013, **5**, 11578–11583.
180 Y. Meng, G. Liu, A. Liu, H. Song, Y. Hou, B. Shin and F. Shan, *RSC Adv.*, 2015, **5**, 37807–37813.
181 R. A. John, A. C. Nguyen, S. Shukla, N. Tiwari, S. Chen, G. I. Ng and N. Mathews, *Chem.*

Mater., 2016, **28**, 8305–8313.
182 D. Sanchez-Rodriguez, H. Eloussifi, J. Farjas, P. Roura and M. Dammak, *Thermochim. Acta*, 2014, **589**, 37–46.
183 P. Roura, J. Farjas, H. Eloussi, L. Carreras, S. Ricart, T. Puig and X. Obradors, *Thermochim. Acta*, 2015, **601**, 1–8.
184 D. Sánchez-Rodriguez, J. Farjas and P. Roura, *Combust. Flame*, 2017, **186**, 211–219.
185 S. Park, K. H. Kim, J. W. Jo, S. Sung, K. T. Kim, W. J. Lee, J. Kim, H. J. Kim, G. R. Yi, Y. H. Kim, M. H. Yoon and S. K. Park, *Adv. Funct. Mater.*, 2015, **25**, 2807–2815.
186 S. Goldstein and J. Rabani, *J. Am. Chem. Soc.*, 2007, **129**, 10597–10601.
187 J. Mack and J. R. Bolton, *J. Photochem. Photobiol. A Chem.*, 1999, **128**, 1–13.
188 T. B. Daunis, D. Barrera, G. Gutierrez-Heredia, O. Rodriguez-Lopez, J. Wang, W. E. Voit and J. W. P. Hsu, *J. Mater. Res.*, 2018, **33**, 2454–2462.
189 B.-Y. Su, S.-Y. Chu, Y.-D. Juang and H.-C. Chen, *Appl. Phys. Lett.*, 2013, **102**, Article No. 192101.
190 Y. J. Kim, J. K. Jeong, J. H. Park, B. J. Jeong, H. D. Lee and G. W. Lee, *Jpn. J. Appl. Phys.*, 2018, **57**, 4–8.
191 J. Hwang, K. Lee, Y. Jeong, Y. U. Lee, C. Pearson, M. C. Petty and H. Kim, *Adv. Mater. Interfaces*, 2014, **1**, Article No. 1400206.
192 J. He, D. M. Weekes, W. Cheng, K. E. Dettelbach, A. Huang, T. Li and C. P. Berlinguette, *J. Am. Chem. Soc.*, 2017, **139**, 18174–18177.
193 J. Leppäniemi, K. Eiroma, H. Majumdar and A. Alastalo, *ACS Appl. Mater. Interfaces*, 2017, **9**, 8774–8782.
194 J. Jo, Y. Kim, J. Park, J. S. Heo, S. Hwang, W. Lee, M. Yoon, M. Kim and S. K. Park, *ACS Appl. Mater. Interfaces*, 2017, **9**, 35114–35124.
195 W. Xu, H. Li, J.-B. Xu and L. Wang, *ACS Appl. Mater. Interfaces*, 2018, **10**, 25878–25901.
196 K. K. Banger, Y. Yamashita, K. Mori, R. L. Peterson, T. Leedham, J. Rickard and H. Sirringhaus, *Nat. Mater.*, 2011, **10**, 45–50.
197 W. T. Park, I. Son, H. W. Park, K. B. Chung, Y. Xu, T. Lee and Y. Y. Noh, *ACS Appl. Mater. Interfaces*, 2015, **7**, 13289–13294.
198 J. Chang, K. L. Chang, C. Chi, J. Zhang and J. Wu, *J. Mater. Chem. C*, 2014, **2**, 5397–5403.
199 K. C. Fairley, D. R. Merrill, K. N. Woods, J. Ditto, C. Xu, R. P. Oleksak, T. Gustafsson, D. W. Johnson, E. L. Garfunkel, G. S. Herman, D. C. Johnson and C. J. Page, *ACS Appl. Mater. Interfaces*, 2016, **8**, 667–672.
200 K. N. Woods, M. C. Thomas, G. Mitchson, J. Ditto, C. Xu, D. Kayal, K. C. Frisella, T. Gustafsson, E. Garfunkel, Y. J. Chabal, D. C. Johnson and C. J. Page, *ACS Appl. Mater. Interfaces*, 2017, **9**, 37476–37483.
201 K. H. Lim, J. E. Huh, J. Lee, N. K. Cho, J. W. Park, B. Il Nam, E. Lee and Y. S. Kim, *ACS Appl. Mater. Interfaces*, 2017, **9**, 548–557.
202 K. Okamura and H. Hahn, *Appl. Phys. Lett.*, 2010, **97**, Article No. 153114.
203 S. Polster, M. P. M. Jank and L. Frey, *J. Appl. Phys.*, 2016, **119**, Article No. 024504.
204 S. R. Thomas, P. Pattanasattayavong and T. D. Anthopoulos, *Chem. Soc. Rev.*, 2013, **42**, 6910–23.
205 Y. S. Rim, H. S. Lim and H. J. Kim, *ACS Appl. Mater. Interfaces*, 2013, **5**, 3565–3571.
206 Y. S. Rim, H. Chen, Y. Liu, S. H. Bae, H. J. Kim and Y. Yang, *ACS Nano*, 2014, **8**, 9680–9686.
207 E. Carlos, R. Branquinho, A. Kiazadeh, P. Barquinha, R. Martins and E. Fortunato, *ACS*

Appl. Mater. Interfaces, 2016, **8**, 31100–31108.
208 K. Song, W. Yang, Y. Jung, S. Jeong and J. Moon, *J. Mater. Chem.*, 2012, **22**, 21265–21271.
209 S. Y. Je, B. G. Son, H. G. Kim, M. Y. Park, L. M. Do, R. Choi and J. K. Jeong, *ACS Appl. Mater. Interfaces*, 2014, **6**, 18693–18703.
210 Y. Zhao, K. Kita and A. Toriumi, *Appl. Phys. Lett.*, 2010, **96**, 2001–2004.
211 J. T. Anderson, W. Wang, K. Jiang, T. Gustafsson, C. Xu, E. L. Gafunkel and D. A. Keszler, *ACS Sustain. Chem. Eng.*, 2015, **3**, 1081–1085.
212 C. K. Perkins, R. H. Mansergh, D. H. Park, C. E. Nanayakkara, J. C. Ramos, S. R. Decker, Y. Huang, Y. J. Chabal and D. A. Keszler, *Solid State Sci.*, 2016, **61**, 106–110.
213 T. B. Daunis, J. M. H. Tran and J. W. P. Hsu, *ACS Appl. Mater. Interfaces*, 2018, **10**, 39435–39440.
214 K. Banger, C. Warwick, J. Lang, K. Broch, J. E. Halpert, J. Socratous, A. Brown, T. Leedham and H. Sirringhaus, *Chem. Sci.*, 2016, **7**, 6337–6346.